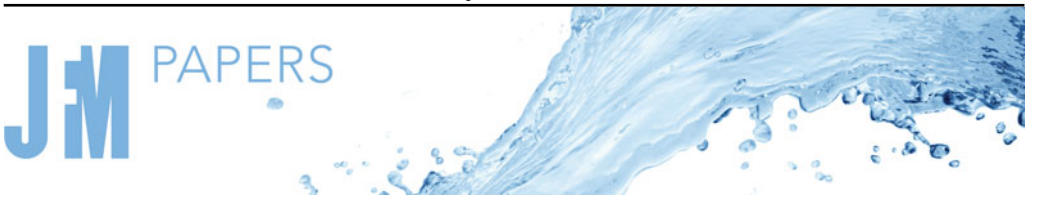
J. Fluid Mech. (2026), *vol.* 1036, A10, doi:10.1017/jfm.2026.11588



Waves in a shear flow: transition between the KH, Holmboe and Miles instability

Anil Kumar[1], **S. Ravichandran**[2] **and Ratul Dasgupta**[1]

[1]Department of Chemical Engineering, Indian Institute of Technology Bombay, Mumbai, Maharashtra 400 076, India

[2]Centre for Climate Studies, Indian Institute of Technology Bombay, Mumbai, Maharashtra 400 076, India

Corresponding authors: Ratul Dasgupta, dasgupta.ratul@gmail.com; S. Ravichandran, sravichandran@iitb.ac.in

(Received 24 July 2025; revised 11 March 2026; accepted 21 April 2026)

We study the generation of waves at the interface of two immiscible fluids, arising due to shear-driven, inviscid instabilities. The background profile is chosen to be the classic exponential velocity profile (Morland & Saffman, *J. Fluid Mech.*, 1993, vol. 252, pp. 383–398) with a sharp density interface (stable stratification). At low Froude ($\sim O_m(1)$) and high Bond numbers ($\sim O_m(100)$), relevant to geophysical and astrophysical situations, we demonstrate a novel (smooth) transition for the fastest growing mode: from the Kelvin–Helmholtz (KH) instability at density ratio $\delta = 0.9$ (ratio of upper to lower fluid densities) to the Holmboe (H) instability as $\delta \to 0.5$ and onwards to the Miles (*J. Fluid Mech.*, 1957, vol. 3, issue 2, pp. 185–204) critical layer instability as $\delta \to 0.001$ (air–water). Notably, the Miles fastest growing mode with its (characteristic) sharp jump in (inviscid) Reynolds stress (τ) at the critical location, persists up to $\delta = 0.01$ i.e. up to ten times the air–water value. The vertical (z) variation of the Reynolds stress (fastest mode), displays a qualitative change with increasing δ; transitioning from having a sharp jump at the critical location for $\delta \ll 1$ (Miles) to smooth variation through this location for $\delta \geqslant 0.5$ (H). A theoretical explanation for this is presented. In the higher density ratio regime ($0.5 \leqslant \delta \leqslant 0.9$), by comparing against stability results from the corresponding piecewise linear (PL) velocity profile, we show the possibility of the H and the KH instability in the exponential model. Simulations, solving the incompressible Euler's equation with gravity and surface tension are reported. In the Miles regime ($\delta = 0.01$) excellent agreement with linear theory upto five wave periods is observed. As these waves saturate, tiny surface ripples appear. Increasing δ to 0.1, finite-amplitude waves resulting from the instability display larger-amplitude ripples on their surface; these are reminiscent of Stokes waves with capillary effects. With further increase ($\delta = 0.5$), exponentially growing waves display a sheared cusp at the crest in the nonlinear regime. They emit spume droplets and resemble the asymmetric H waves in the simulations and experiments of Lawrence *et al.* (1998). At $\delta = 0.9$, growing interfacial waves rapidly distort into classic KH spirals within five wave periods. Several comparisons reported between the PL and the exponential

© The Author(s), 2026. Published by Cambridge University Press.

https://doi.org/10.1017/jfm.2026.11588 Published online by Cambridge University Press

profile clarify the role of background profile curvature and the critical location. To our knowledge, this is the first demonstration of three canonical instabilities, within these background states and without usage of the Boussinesq approximation.

Key words: shear-flow instability, surface gravity waves

1. Introduction

Shear generated surface or internal waves in density stratified flows, particularly at high Reynolds numbers, have occupied a central space in hydrodynamic stability research since the pioneers (Helmholtz 1868; Rayleigh 1895; Thomson 1871; Taylor 1931; Goldstein 1931). That important outstanding problems persist, attest to the complexity of the subject and highlight its relevance to wide ranging situations of geophysical, astrophysical or industrial interest. Adverse effects of climate change seemingly call for renewed attention into geophysical problems involving surface and internal waves; this is so because processes accompanying these often generate complicated, multiscale phenomena, both in the ocean and the atmosphere with long-term climate consequences. Examples include wave breaking (surface or internal gravity waves in the ocean and atmosphere) and associated mixing (Peltier & Caulfield 2003, section 6.2.1 in Fritts & Alexander 2003 etc.) or ocean spray generation (Deike 2022). Due to the multiscale nature, parameterisation of some of these processes in large-scale numerical models of wave or climate is necessary (Staquet & Sommeria 2002; Cavaleri *et al.* 2007; Janssen 2008; Perlin, Choi & Tian 2013) and in turn calls for accurate knowledge of the micro-physics. We refer the reader to figure 9 in Garrett & Munk (1979) (figure 5 in Thorpe 1975) for a caricature of some of these processes in the ocean.

The mechanism through which an overlying, moving gas or a liquid raises waves at the interface of an underlying, immiscible liquid layer (the common example being wind blowing over the deep ocean) has been of near constant interest since (1925); see Pizzo, Deike & Ayet (2021) for a recent summary and Mitsuyasu (2002) for a historical overview of the wind-wave problem. The configuration also applies to industrial situations involving gas–liquid (Matas, Marty & Cartellier 2011) or liquid–liquid combinations involving thick or thin films (Cohen & Hanratty 1965; Boomkamp & Miesen 1996) subject to shear. Our interest here is restricted to the regime of geo/astro-physical interest involving two fluid layers (gas–liquid or liquid–liquid depending on the density ratio) with shear in the upper layer and a sharp density jump. Such a configuration is of oceanic interest at low density ratio (air–water) (Miles 1957) and of astrophysical as well as geophysical interest at higher values (Pouliquen, Chomaz & Huerre 1994; Alexakis, Young & Rosner 2002). In the base state (also referred to as the 'background state') depicted in figure 1, a shear profile is imposed in the upper layer (the exponential velocity profile studied first in Morland & Saffman (1993) with a sharp density interface at $z = 0$, representative of a quasi-laminar wind profile), with quiescent lower fluid (stable density stratification). We study the linear stability of this configuration analytically and the time evolution of the most unstable mode computationally, within the inviscid framework, accounting for gravity and surface tension. Our analysis is restricted to unstable waves sufficiently long compared with the shear layer thickness (i.e. the background vorticity layer) as well as relevant capillary and viscous length scales (we return to viscous effects at the end of the study), but sufficiently short such that the deep layer approximation remains applicable. Within these simplifying approximations, we study transition in the nature of the fastest growing mode in the non-dimensional space comprising Froude number (Fr) (ratio of inertia to gravity) and density

https://doi.org/10.1017/jfm.2026.11588 Published online by Cambridge University Press

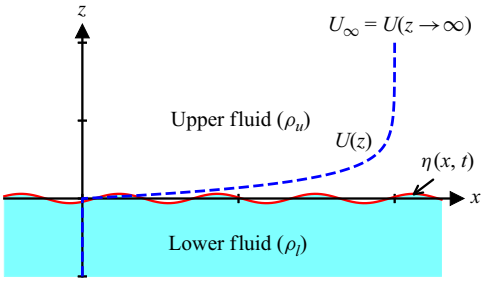


Figure 1. Exponential velocity profile with quiescent fluid below, in the base (background) state with upper fluid velocity varying as $U_u(z) = U_\infty[1 - \exp(-z/\Delta)]$. A sharp interface separates two fluids of differing densities in a statically stable configuration: $\rho(z) = \rho_l,\ z < 0$ and $\rho(z) = \rho_u,\ z > 0$ with $\rho_l > \rho_u$.

ratio (δ) (upper to lower fluid), at a large Bond ($Bo \gg 1$) number (ratio of gravity to surface tension). The precise definitions of these non-dimensional numbers are introduced in § 2.

The key result of our study is the demonstration, at high Bond number and moderately low Froude number, of a novel transition (for the fastest growing mode) from the Kelvin–Helmholtz (KH) (Thomson 1871; Helmholtz 1868) to the Holmboe (H) instability (Holmboe 1962) and eventually to the Miles (Miles 1957) critical layer instability, as the density ratio is reduced from 0.9 through 0.5 to the air–water value (0.001). While transition from the KH to the H instability (Smyth & Peltier 1989; Lawrence, Browand & Redekopp 1991, 1998; Smyth & Winters 2003) for other background profiles or from the Miles to the KH instability (Morland & Saffman 1993; Alexakis *et al.* 2004*a*) for the current profile have been reported, we demonstrate here the occurrence of all three aforementioned, inviscid, shear instabilities within the single base-state model of figure 1; to our knowledge, this is the first such demonstration.

Our analytical results receive support from comparison of the temporal evolution of the interface shape, obtained through solving the nonlinear, inviscid equations of motion. Simulations conducted using the open-source code Basilisk (Popinet & Collaborators 2013–2025) show very good agreement with theoretical predictions in the linear regime. In the nonlinear regime, we note qualitative differences between the KH spirals (at $\delta = 0.9$) and contrast these to sheared, cusp-like interface deformation emitting spume droplets for H-like ($\delta = 0.5$) waves; these numerical observations are consistent with the numerical and experimental observations of Lawrence, Haigh & Zhu (1998) distinguishing the KH from the H instability for asymmetric velocity profiles. At $\delta = 0.1$, simulations display features in the nonlinear regime, reminiscent of ripples on finite-amplitude, capillary-gravity Stokes waves. Their appearance typically accompanies an abrupt reduction of the parent wave amplitude. In the rest of this study, we refer to waves appearing for $\delta \gg 0.1$ as internal waves consistent with experimental literature (Mercier, Vasseur & Dauxois 2011). The analysis of Yih (1960) showed that waves on a surface of density discontinuity are a limiting case of internal (gravity) waves appearing in continuously, stratified flows, thus supporting this nomenclature. In contrast, at very low density ratios ($\ll 0.1$), we describe surface waves.

1.1. *Literature review*

In the low density ratio regime (air–water, $\delta = 0.001$), linear stability of the base state of figure 1 has been studied by several authors for a range of Froude and Bond numbers. For example, refer to Morland & Saffman (1993), Leblanc (2007), Carpenter, Guha & Heifetz (2017), Bonfils *et al.* (2022), Kadam, Patibandla & Roy (2023) for linear stability

https://doi.org/10.1017/jfm.2026.11588 Published online by Cambridge University Press

studies with distinct perspectives and to Leblanc (2007), Leblanc (2007) for weakly nonlinear investigations; these studies are relevant to wind-driven, water waves with $\delta = 0.001$. Apparently, situations involving immiscible fluids subject to shear at density ratios significantly higher than the air–water value also occur commonly. Fresh and salt water, for example, have a density ratio >0.95; a sharp interface is maintained on experimental time scales between the two; see Mercier *et al.* (2011). Pouliquen *et al.* (1994) studied the KH and H instability experimentally using fluids of a high density ratio ~ 0.92 (water and equal mixture of silicone oil with 1–2–3–4-tetrahydronaphthalene; see their table 1), comparing their experimental results against inviscid stability theory. That an inviscid theory suffices to describe their experimental results involving somewhat viscous fluids is justified from the estimate of the viscous diffusion time scale on p. 282 of Pouliquen, Chomaz & Huerre (1994) along with the Reynolds number (see p. 293). Beyond geophysical scales, Alexakis *et al.* (2002) report that a density ratio of 0.1 in shear flows occurs in astrophysical situations involving accretion from a normal star to a white dwarf star; see the discussion on pp. 1–2 of Alexakis *et al.* (2002).

To our knowledge, the only analytical study of the stability of the exponential profile of figure 1 at a larger density ratio (compared with air–water) has been carried out by Alexakis *et al.* (2002, 2004*a*). These authors studied the moderately low Froude number and large wavenumber limit theoretically, obtaining an analytical expression for the growth rate (in the linear regime) at an arbitrary density ratio; no analysis of the nature of the instability or any transition therein with varying density ratio was reported, as is done here. Alexakis, Young & Rosner (2004*b*) studied the weakly nonlinear regime for a small Froude number (the weak wind limit) and small density ratio, obtaining amplitude equations that were then solved numerically. These solutions validated the prediction (Haberman 1972) that, for a growing mode (Miles 1957), the phase change across the critical layer expected from linear theory saturates to zero as the wave amplitude increases with time. The nonlinear simulations by Alexakis *et al.* (2004*a*) were however in the moderate-Froude-number $Fr = 2.3-9.5$ and low-Mach-number regime, at a fixed density ratio of 0.1. Qualitative agreement with linear theory was reported for the growth of gravitational potential energy of unstable Fourier mode(s), although significant scatter is apparent in their comparison; see Alexakis *et al.* (2004*a*, Figure 4). At these Froude numbers, the authors reported regimes separating the Miles from the KH instability, although their KH model is similar to that in figure 2(*b*) with a jump at the interface, and not the more general continuous and piecewise linear (PL) model of figure 2(*a*). We will demonstrate later on that at $\delta = 0.1$ (as is the case for Alexakis *et al.* 2004*a*) and low Froude number, the instability in the exponential model of figure 1 begins to lose its signature at the critical location, indicative of a potential change in the instability mechanism.

We note the important study by Morland & Saffman (1993), which explored transitions from the Miles instability to the discontinuous KH instability in the exponential model, at a low (air–water) density ratio and for a large Fr and infinite Bond number. Importantly, they proved the continuation of the Howard semi-circle theorem to shear flow with a sharp density interface; this had been done by Yih (1972) albeit for surface waves ($\delta = 0$) and also subsequently by Alexakis *et al.* (2002) for arbitrary δ. In § 3.1 we will see that even at $Fr \sim 3000 \gg 1$, the growth rate of the fastest growing mode in the exponential model agrees much better with that of the PL model (figure 2*a*) rather than the discontinuous KH model of figure 2(*b*) considered by Morland, Saffman & Yuen (1991) and Alexakis *et al.* (2002). With this brief survey above, it becomes clear that the nature of the linear instability for the exponential model of figure 1 as a function of the density ratio and transitions, if any, for the fastest growing mode are not known. This is demonstrated in the present study by employing theory and numerical simulations.

https://doi.org/10.1017/jfm.2026.11588 Published online by Cambridge University Press

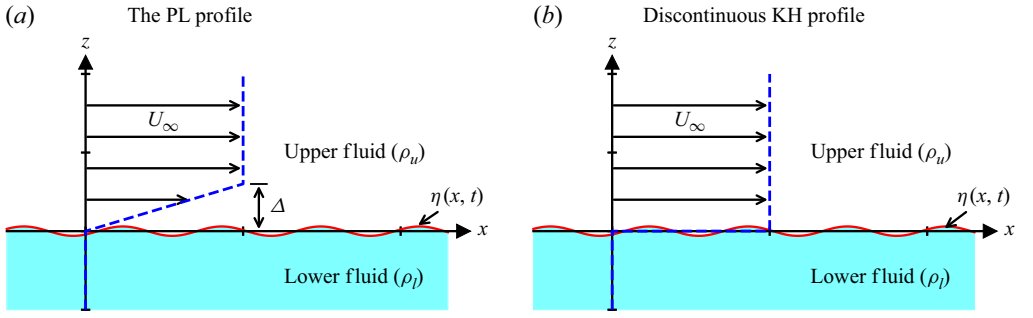


Figure 2. (*a*) The PL profile with a shear layer of thickness Δ. The upper fluid background velocity is given by $U_u(z) = U_\infty(z/\Delta),\ 0 \leqslant z \leqslant \Delta$ and $U_u(z) = U_\infty,\ z \geqslant \Delta$. (*b*) The classic KH discontinuous profile, obtained when $\Delta \to 0$ in the PL profile in panel (*a*). In both panels, the lower fluid is quiescent in the base state, i.e. $U_l(z) = 0,\ z < 0$. The statically stable, base-state density profile is $\rho(z) = \rho_l,\ z < 0$ and $\rho(z) = \rho_u,\ z > 0$ with $\rho_l > \rho_u$.

1.2. *Inviscid, shear instabilities and the exponential model*

For the exponential profile in figure 1, the background shear layer thickness is approximately $\approx \Delta$. With a sharp density interface placed within this shear layer, three inviscid instabilities can potentially manifest, depending on the parameter regime. Two of these (the KH and H), are approximately understood using PL velocity profiles (their continuations to smooth profiles also being well known) while for the third instability (Miles 1957), curvature of the background velocity profile is crucial. For completeness, we recap some salient features.

Recall that the KH instability occurs through an inflexional instability mechanism (see discussion on pp. 277−278 of Pouliquen *et al.* (1994) applicable to a homogeneous fluid under shear (i.e. no stratification). The textbook KH profile is usually the base state of figure 2(*b*) (a vortex sheet), representing the limiting case of an inflectional velocity profile (Michalke 1964) such as a tanh profile; the vortex sheet of figure 2(*b*) is unstable to all wavenumbers when the density ratio ($\delta \equiv \rho_u/\rho_l$) is unity. Density stratification plays a stabilising role for the sheet – only sufficiently large wavenumbers are unstable when $0 < \delta < 1$. The KH instability can also manifest in the PL model of figure 2(*a*) for perturbations whose wavelength λ is large compared with the shear layer thickness ($\lambda \gg \Delta$). By replacing the smooth, background vorticity gradient ($\mathrm{d}^2U_u/\mathrm{d}z^2$) of figure 1 with the apparently simpler PL profile of figure 2(*a*) with a jump in background vorticity at $z = \Delta$, the KH instability can also be interpreted as resonance between waves on the two vorticity interfaces at $z = 0$ and $z = \Delta$; see discussion around figure 1 in Baines & Mitsudera (1994) and around equation 33 in Carpenter *et al.* (2011) for smooth profiles.

In contrast to the KH instability, the H instability (Holmboe 1962) occurs due to the destabilising influence of stable stratification under shear, manifesting in situations where the thickness of the shear layer is much larger than that of the density layer. Employing the same PL profile of figure 2(*a*), one can interpret the H instability as resonance between a wave on the density and that on the vorticity interface(s); see figure 16(*d*) in Carpenter *et al.* (2011). The difference between the H and KH instability is seen most readily when the centre of the shear layer coincides with the density interface (symmetric profiles) leading to stationary (KH) and travelling (H) modes. The profiles of figures 1 and 2(*a*) however are asymmetric, the latter represents a limiting case of the profile in Lawrence, Browand & Redekopp (1991) and we will return to this asymmetry later in our study.

https://doi.org/10.1017/jfm.2026.11588 Published online by Cambridge University Press

The third instability admissible for the profile of figure 1 is the critical layer instability of Miles (1957). Although the Rayleigh equation is strictly not singular at any real value of the vertical coordinate z for a growing mode with complex c, for our present study, we define the critical location as the (real) location z_c where $U_u(z = z_c) = c_r(k)$ (c_r denotes the real part of the phase speed c), this being done for unstable modes. Unlike the H and KH instabilities, non-zero curvature of the background profile at the critical location is crucial to the instability (see below). This instability, more broadly, belongs to the 'class B' family of instabilities of Benjamin (1960, 1963). As explained in Benjamin (1960) last paragraph on p. 514), the instability 'takes the form of waves progressing in the flow direction at very nearly the same speed as free surface waves in the flexible medium, the waves being amplified by the action of the flow which supplies sufficient energy to counterbalance internal dissipation'. At low density ratio, Miles (1957) demonstrated that, for this instability, the growth rate of a Fourier mode is proportional to $(-\mathrm{d}^2U_u/\mathrm{d}z^2)_{z_c}$, $U_u(z)$ being the background shear flow in the upper fluid (subscript 'u' for upper). In regimes where this critical location dominates the instability mechanism, we will verify that for the fastest growing Fourier mode, a near-discontinuous jump in the (inviscid) Reynolds stress appears at the critical location and upto the interface (also see figure 2 in Boomkamp & Miesen (1996). (We recall that the critical layer plays a crucial role in the viscous instability of non-inflectional, velocity profiles in unstratified, parallel shear flows, e.g. the plane Poiseuille flow (Lighthill & Rosenhead (1963) figure *IX*.8.) or TS instability of the Blasius boundary layer (Ruban, Gajjar & Walton (2023) 2). The associated work done by this shear stress leads to extraction of energy from the background shear primarily in the region between the critical location and the interface. This will be contrasted against situations where the energy extraction occurs in the entire shear layer with no distinct signature of the Reynolds stress at the critical location; this is despite the mathematical existence of a critical location for every growing Fourier mode, as ensured by the semi-circle theorem.

While we have discussed the three instabilities above in an apparent mutually exclusive manner, critical locations appear within the inviscid framework (Taylor–Goldstein equation) for the KH as well as H instabilities with smooth velocity (and density) profiles. Refer to figures 5 and 7 in Smyth & Peltier (1989), where phase jumps and peaks are seen at the critical location for the eigenfunction and the Reynolds stress for unstable KH and H modes, respectively. We bear this aspect in mind when distinguishing between critical layer Miles instabilities at low density ratios and H and KH instabilities at higher values. In addition, comparison of instabilities obtained from curved background profiles (figure 1) with their straight line counterparts (figure 2), as is done throughout our study, despite being common, requires caution; see, e.g. Morland *et al.* (1991) for the distinction in the transition mechanism between instability in the PL profile and that of the exponential profile for a sheared lower fluid ($\delta = 0$). For background profiles with a smooth second derivative, the logarithmic singularity in Tollmien's inviscid solution (applicable to a neutral mode, provided such a mode exists) gets regularised and spread over a finite thickness for a growing mode. Note that the neutral mode is singular at a (real) z where the second derivative of the background profile is non-zero and the modal phase speed matches the background speed. Interestingly, it is possible to describe this critical layer region via kinks present in PL profiles; a large number of kinks being necessary for an accurate representation; see Carpenter *et al.* (2017). Closely related to our study, we also note the interesting study by Eaves & Balmforth (2019), where several diagnostics, both analytical and numerical, in order to distinguish the Taylor-Caulfield instability from the H and KH instability are discussed.

https://doi.org/10.1017/jfm.2026.11588 Published online by Cambridge University Press

This study is organised as follows. In § 2 we discuss the temporal, linear stability of the exponential profile in figure 1 obtaining the dispersion relation. The same is also done for the PL profile in figure 2(*a*). Section 3 presents a detailed exploration of the parameter space for high and low Froude numbers with increasing density ratio, for high Bond numbers. Section 4 presents numerical simulations validating linearised predictions but also presenting several novel results in the nonlinear regime. In § 5 we revisit the validity of the background state of figure 1, particularly for higher density ratios, close to unity. We conclude with a summary in § 6.

2. Temporal, linear stability analysis

The base state (figure 1) comprises a stably stratified ($\rho_l > \rho_u$) configuration with a sharp density jump at $z = 0$ and shear (only) in the upper fluid:

$$U(z) = \begin{cases} U_u(z) = U_\infty \left(1 - \exp\left(-\dfrac{z}{\Delta}\right)\right), & z > 0, \\ U_l(z) = 0, & z < 0, \end{cases} \tag{2.1a}$$

$$\rho(z) = \begin{cases} \rho_u, & z > 0, \\ \rho_l, & z < 0. \end{cases} \tag{2.1b}$$

In the base state the interface is flat at $z = 0$. The perturbed state is represented by the streamfunctions $\psi_u(x, z, t)$ and $\psi_l(x, z, t)$ (for the upper and lower fluid, respectively), while the deviation of the interface from its flat state is measured by $\eta(x, t)$ (see figure 1). The vertical variation of the perturbation streamfunction ($\Psi_{u/l}$) is governed by the Rayleigh equations below (subscripts u or l refer to upper and lower layers, respectively):

$$\left\{U_{u/l}(z) - c(k)\right\}\left(D^2 - k^2\right)\Psi_{u/l}(z) - D^2 U_{u/l}(z)\Psi_{u/l}(z) = 0. \tag{2.2a,b}$$

Here $D \equiv \mathrm{d}/\mathrm{d}z$ and $\Psi_{u/l}(z)$ is related to the streamfunction $\psi_{u/l}(x, z, t)$ via a travelling wave, Fourier mode representation, *viz.* (we omit the u or l subscripts below)

$$\psi(x, z, t) = \frac{1}{2}\Psi(z)\exp\left[ik(x - ct)\right] + \text{c.c.}, \quad u \equiv \frac{\partial \psi}{\partial z}, \quad w \equiv -\frac{\partial \psi}{\partial x}. \tag{2.3}$$

Here $i \equiv \sqrt{-1}$, u and w are the horizontal and vertical, perturbed velocity components, respectively, while c.c. denotes the complex conjugate. The perturbed interface (vertical displacement) is similarly represented using complex notation as

$$\eta(x, t) = \frac{1}{2}\eta_0 \exp\left[ik(x - ct)\right] + \text{c.c.}, \tag{2.4}$$

where η_0 is a complex constant. Equation (2.2) represents eigenvalue problems for determining complex functions $\Psi_u(z)$, $\Psi_l(z)$ and $c(k)$ subject to boundary conditions (see below) for the chosen base-state profile in (2.1) and for real k. The boundary conditions are the (linearised) kinematic boundary condition

$$c\eta_0 = \Psi_u(0) = \Psi_l(0), \tag{2.5a,b}$$

and the jump in normal stress (pressure in the inviscid framework here) due to surface tension (T) is

$$P_u(0) - P_l(0) = (\rho_u - \rho_l)\, g\eta_0 - Tk^2\eta_0, \tag{2.6}$$

where $p(x, z, t) = (1/2)P(z)\exp[i(kx - ct)] + \text{c.c.}$ is the perturbation pressure (with appropriate subscripts). The expressions relating the perturbation streamfunction $\Psi(z)$ to

https://doi.org/10.1017/jfm.2026.11588 Published online by Cambridge University Press

the vertically varying part of the perturbation pressure ($P(z)$) are

$$P_u(0) = -\rho_u \left[(U_u(z) - c) D\Psi_u - (DU_u)\,\Psi_u\right]_{z=0}, \quad P_l(0) = c\rho_l \left(D\Psi_l\right)_{z=0}. \quad (2.7a,b)$$

In addition to the boundary conditions above, it is also necessary to ensure that the solution to (2.2) does not diverge as $z \to \pm\infty$ and this determines two constants of integration in expressions for $\Psi_l(z)$ and $\Psi_u(z)$. As shown by J. Miles in Morland & Saffman (1993), see Russell (1994, § 3.3) for details, the Rayleigh equation for the upper fluid may be converted into the Gauss hypergeometric equation whose analytical properties are well known. The Rayleigh equation for the lower fluid has constant coefficients and is thus straightforward to solve. We thus obtain expressions for the perturbation streamfunction in both fluids as

$$\Psi_u(z) = M \;\exp\left[-k\,(z - z_c)\right]\; {}_2F_1\left(\alpha, \beta, \gamma; \frac{\exp\left(-\dfrac{z}{\Delta}\right)}{1 - \dfrac{c}{U_\infty}}\right), \quad \Psi_l(z) = N \exp\left(kz\right), \quad (2.8a,b)$$

with $\alpha \equiv k\Delta + \sqrt{1 + k^2\Delta^2}$, $\beta \equiv k\Delta - \sqrt{1 + k^2\Delta^2}$ and $\gamma \equiv 1 + 2k\Delta$, where M and N are (complex) constants of integration. In (2.8*a*), ${}_2F_1(\cdot, \cdot, \cdot; \cdot)$ is the Gauss hypergeometric function defined by the series

$${}_2F_1(\alpha, \beta, \gamma; t) = 1 + \frac{\alpha\beta}{\gamma}\frac{t}{1!} + \frac{\alpha\,(\alpha+1)\,\beta\,(\beta+1)}{\gamma\,(\gamma+1)}\frac{t^2}{2!} + \cdots, \qquad |t| < 1. \quad (2.9)$$

Note that with $t \equiv \exp(-z/\Delta)/(1 - (c/U_\infty))$, as z varies in the range $\infty < z \leqslant z_c$, we have the variation $0 < t \leqslant 1$ assuming that z_c is real (for a neutral mode) and determined using $U_u(z_c) = c(k)$. For the range $0 \leqslant z \leqslant z_c \Rightarrow (U_\infty/(U_\infty - c_r)) \geqslant t \geqslant 1$ assuming that $c < U_\infty$. This necessitates the continuation of ${}_2F_1(\cdot, \cdot, \cdot; t)$ for $|t| > 1$ for which, for example, the Euler's integral representation of ${}_2F_1$ may be used (see further discussion in Andrews *et al.* 1999, p. 65):

$${}_2F_1(\alpha, \beta, \gamma; t) \equiv \frac{\Gamma(\gamma)}{\Gamma(\beta)\Gamma(\gamma - \beta)} \int_0^1 \frac{r^{\beta-1}(1-r)^{\gamma-\beta-1}}{(1 - rt)^\alpha}\,\mathrm{d}r. \quad (2.10)$$

Using the kinematic boundary condition (2.5*a*,*b*) in (2.8), we obtain

$$\Psi_u(z) = c\eta_0 \exp\left(-kz\right)\left[\frac{{}_2F_1\left(\alpha, \beta, \gamma; \dfrac{\exp\left(-\dfrac{z}{\Delta}\right)}{1 - \dfrac{c}{U_\infty}}\right)}{{}_2F_1\left(\alpha, \beta, \gamma; \dfrac{1}{1 - \dfrac{c}{U_\infty}}\right)}\right], \quad \Psi_l(z) = c\eta_0 \exp\left(kz\right). \quad (2.11a,b)$$

We also note that $t = 1$ is a branch point of ${}_2F_1(\alpha, \beta, \gamma; t)$; this generates a (near) jump in phase of the streamfunction $\Psi_u(z)$ in (2.11*a*) for a Miles growing mode (i.e. a k for which $\mathrm{Im}(c) = c_i > 0$), as the critical location z_c is crossed ($t = 1^+$). This in turn also generates the phase shift in perturbation pressure at $z = 0^+$ compared with the interface η. This phase shift produces the Jeffreys (1925) mechanism of generating wind waves, extensively referred to in Miles (1957).

https://doi.org/10.1017/jfm.2026.11588 Published online by Cambridge University Press

Using expressions for $\Psi_u(z)$ and $\Psi_l(z)$ from (2.11) in (2.7) and the normal stress condition in (2.6), we obtain the following dispersion relation. In non-dimensional form, this may be expressed as

$$\left[\delta\left\{\kappa-\left(\frac{1}{1+2\kappa}\right)\left(\frac{Fr}{Fr-\tilde{c}}\right)\frac{{}_2F_1\left(\alpha+1,\beta+1,\gamma+1;\frac{Fr}{Fr-\tilde{c}}\right)}{{}_2F_1\left(\alpha,\beta,\gamma;\frac{Fr}{Fr-\tilde{c}}\right)}\right\}+\kappa\right]\tilde{c}^2 \quad (2.12)$$
$$-\delta Fr\tilde{c}-(1-\delta)-\frac{1}{Bo}\kappa^2=0,$$

where

$$\tilde{c}\equiv\frac{c}{\sqrt{g\Delta}},\ \kappa\equiv k\Delta,\ Fr\equiv\frac{U_\infty}{\sqrt{g\Delta}},\ \delta\equiv\frac{\rho_u}{\rho_l},\ Bo\equiv\frac{\rho_l g\Delta^2}{T}. \quad (2.13)$$

Here Fr, Bo and δ represent the Froude number, Bond number and the density ratio, respectively. For a given κ (wavenumber), the complex roots ($\tilde{c}$) to (2.12) are obtained numerically using the *findroot* function from the *mpmath* library (Johansson 2024) in Python, which provides arbitrary-precision root finding based on Muller's method (Müller 1956). In the supplementary material (§ 1) we provide benchmarking with the results of Morland & Saffman (1993) and Young & Wolfe (2014) for validation of the numerical procedure of solving (2.12). In the following sections, we extensively use the symbols c_g, c_{gc} and c_{KH} whose formulae are provided below in the deep limit.

Unsheared surface-gravity wave speed: $$c_g^2\equiv\left(\frac{1-\delta}{1+\delta}\right)\frac{g}{k}. \quad (2.14a)$$

Unsheared capillary-gravity wave speed : $$c_{gc}^2\equiv\left(\frac{1-\delta}{1+\delta}\right)\frac{g}{k}+\frac{Tk}{\rho_l\,(1+\delta)}. \quad (2.14b)$$

The KH wave speed: $$c_{KH}\equiv\left(\frac{\delta}{1+\delta}\right)U_\infty. \quad (2.14c)$$

3. Exploring the parameter space

In the following analysis, we explore the nature of the instability in the non-dimensional space of Froude number (Fr) and density ratio (δ) for given value(s) of the Bond number (Bo). Wherever relevant, we compare the results of the PL profile of figure 2(a) with that of the exponential profile of figure 1, both profiles chosen to have the same vertical scale Δ. We investigate four representative cases by varying δ and Fr at fixed Bo: (i) high $Fr=3194.38$, low $\delta=0.001$; (ii) high $Fr=3194.38$, high $\delta=0.5$; (iii) moderately low $Fr=4.79$, low $\delta=0.001$; and (iv) moderately low $Fr=4.79$, high $\delta=0.5$. For the benefit of the reader, table 1 summarises key observations, as will be inferred from following analysis. We commence our parametric exploration with the high-Froude-number case with zero surface tension, i.e. the infinite Bond case.

3.1. *Infinite bond ($Bo\to\infty$) and high Froude number ($Fr\gg1$)*

3.1.1. *Low density ratio ($\delta\ll1$):*

To our knowledge the first study that investigated transition in the nature of the instability for the exponential profile of (2.1) with a sharp density jump at $z=0$ was

https://doi.org/10.1017/jfm.2026.11588 Published online by Cambridge University Press

Section	Profile & parameter range	Key result(s)
§ 3.1: high Froude number $\begin{pmatrix} Fr = 3194.38, \\ Bo \to \infty \end{pmatrix}$	§ 3.1.1: PL and exponential model low δ ($\delta = 0.001 \ll 1$)	Growth rate from exponential model matches that of the PL model, but not the discontinuous KH model. Energy extraction of KH mode across entire shear layer.
§ 3.2: moderately low Froude number $\begin{pmatrix} Fr = 4.79, \\ Bo \to \infty \end{pmatrix}$	§ 3.2.1: PL model ($0.001 \leqslant \delta \leqslant 1$)	Transition from H ($\delta = 0.001$) to KH ($\delta = 0.9$) instability with increasing δ – wave resonances as metric.
	§ 3.2.2: exponential model ($0.001 \leqslant \delta \leqslant 1$)	Low δ ($= 0.001$): Miles' instability with phase speed c_g. Sharp jump in Reynolds stress and peak in perturbation kinetic energy at critical location. Energy extraction between critical location and density interface. Increasing ($\delta \gtrsim 0.1$): Reynolds stress smoothens and kinetic energy peak at critical location becomes subdominant. Energy extraction across entire shear layer. Good match with PL model at $\delta = 0.5$ indicative of a Miles to H instability transition.
§ 3.3: moderately low Froude number $\begin{pmatrix} Fr = 4.79, \\ Bo = O_m(88) \end{pmatrix}$	Exponential model ($0.001 \leqslant \delta \leqslant 1$)	Finite but large Bo instabilities: qualitatively similar to those with $Bo \to \infty$
§ 4: nonlinear simulations $\begin{pmatrix} Fr = 4.79, \\ Bo = O_m(88) \end{pmatrix}$	Exponential model	Finite-amplitude waves exhibit surface ripples ($0.01 \leqslant \delta \leqslant 0.1$). Finite-amplitude H waves with cusp-like crests emitting droplets ($\delta = 0.5$). Typical KH spirals ($\delta = 0.9$).

Table 1. Summary of observations based on fastest growing modes.

by Morland & Saffman (1993). These authors solved the Rayleigh equation numerically for the exponential profile (quiescent water in base state) for air–water ($\delta = 0.001$) taking into account gravity but setting surface tension to zero ($Bo \to \infty$). Among other conclusions, Morland & Saffman (1993) noted a change in the nature of the instability at $Fr \gg 1$ (for constant δ), transitioning from 'Miles unstable' (critical layer induced instability) gravity waves with approximate phase speed c_g^2 (in deep water, (2.14*a*)) to KH unstable waves (i.e. waves appearing on the base state of figure 2*b*) with a phase speed given by c_{KH} (2.14*c*). Such KH-like behaviour is anticipated for unstable modes of wavelength λ satisfying $\Delta \ll \lambda < (2\pi U_\infty^2 \delta / g(1 - \delta^2))$ (see discussion below (3.2) in Morland & Saffman (1993)). It is also intuitively clear from examining the exponential profile in (2.1) that taking the limit $\Delta \to 0$ ($Fr \to \infty$) for fixed U_∞, g and density ratio δ, deforms the exponential profile in figure 1 towards a uniform velocity profile (U_∞) in the upper fluid; in other words, the classic KH base-state profile of figure 2(*b*). (For the exponential profile, the $Fr \to \infty$ limit for fixed $\delta \ll 1$ as discussed here is qualitatively different from $\delta \to 0, Fr \to \infty$, with the limits taken in that order; see discussion below equation (7.17) in Young & Wolfe (2014).) In dimensional variables, the dispersion relation for this KH base state is (Drazin & Reid (2004), Equation (4.20))

https://doi.org/10.1017/jfm.2026.11588 Published online by Cambridge University Press

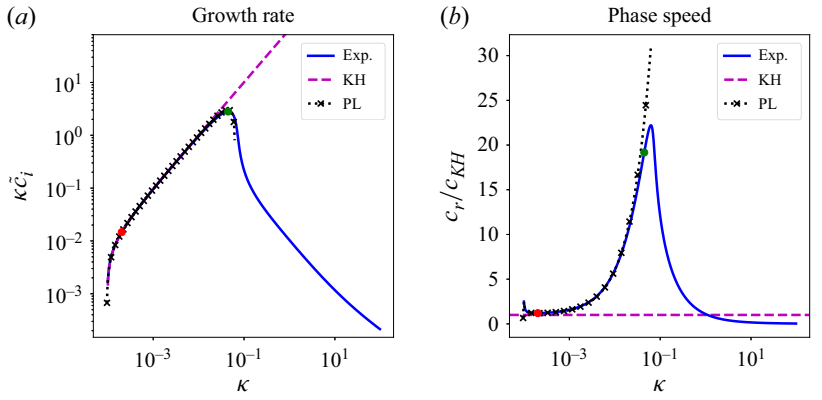


Figure 3. The infinite Bond ($Bo \to \infty$), high Froude ($Fr = 3194.38$) number and low (air–water) density ratio ($\delta = 0.001$) case. (*a*) Growth rate ($\kappa\tilde{c}_i$) and (*b*) phase speed (c_r/c_{KH}) as a function of the non-dimensional wavenumber κ for the KH dispersion relation from (3.1) (pink dashed curve) for the exponential profile (solid blue curve) from (2.12) and for the PL profile from the dispersion relation in (3.2) ('$\cdot \times \cdot$' symbols) for the base states of figures 1 and 2. We see that the growth rate and phase speed are very similar for $\kappa \to 0$. The KH dispersion relation of (3.1) does not contain the Froude number as a parameter and represents the $Fr \to \infty$ limit. The red and green dots in both panels depict a small wavenumber and the fastest growing wavenumber, respectively.

$$\frac{c(k)}{U_\infty} = \frac{\delta}{1+\delta} \pm \left[\left(\frac{1-\delta}{1+\delta} \right) \frac{g}{kU_\infty^2} - \frac{\delta}{(1+\delta)^2} \right]^{1/2}. \tag{3.1}$$

The relation (3.1) predicts that unstable KH modes travel with the speed c_{KH}, independent of wavenumber. At any U_∞, sufficiently long waves are stable (due to gravity), while shorter waves are destabilised by the shear and grow exponentially in time.

We also compare predictions from the dispersion relation (2.12) for the exponential profile in the high-Froude-number limit with that of the PL velocity profile indicated in figure 2(*a*). In terms of the non-dimensional variables and parameters introduced earlier, the dispersion relation (cubic polynomial in $\tilde{c}$) for the PL profile of figure 2(*a*) can be shown to be

$$\begin{aligned} &\left(Fr(1-2\kappa) + 2\tilde{c}\kappa\right) \cdot \left(\frac{1-\delta}{1+\delta}(-2 + \tilde{c}Fr) - \tilde{c}Fr + 2\tilde{c}^2\kappa \right) \\ &\quad + \mathrm{e}^{-2\kappa} \cdot Fr \cdot \left\{ \tilde{c}Fr \left(1 - \frac{1-\delta}{1+\delta} \right) + 2 \left(\frac{1-\delta}{1+\delta} \right) \left(1 - \tilde{c}^2\kappa \right) \right\} = 0, \quad \tilde{c} \neq 0. \end{aligned} \tag{3.2}$$

Plotted in figures 3(*a*) and 3(*b*) are the growth rate and phase speed of the exponential profile (labelled as 'Exp') as obtained from (2.12), for the KH profile from (3.1) and for the PL profile from (3.2), at a high Froude number, *viz.* $Fr = 3194.39$. A few qualitative features are discernible readily. On account of having an additional length scale Δ compared with the classic KH model in figure 2(*b*), the stability characteristics of the PL profile ('$\cdot \times \cdot$' symbols) differ qualitatively at large wavenumbers from the KH model (dashed pink line), as seen in figure 3. Wavenumbers with $\kappa \geqslant O_m(0.1)$ ($\mathcal{O}_m$ denotes order of magnitude) are stable in the PL model – this is the reason for the abrupt termination of the '$\cdot \times \cdot$' symbols (PL model) around $\kappa \sim 10^{-1}$ in figure 3(*a*), above this wavenumber the growth rate goes to zero rapidly. For the exponential profile, also recall that a lower cutoff in wavenumber exists at infinite depth (Young & Wolfe (2014), Kadam *et al.* (2023)); wavenumbers less than this cutoff are stable (Young & Wolfe 2014) as seen from the abrupt decay in growth rate in figure 3(*a*) at low κ.

https://doi.org/10.1017/jfm.2026.11588 Published online by Cambridge University Press

Figures 3(*a*) and 3(*b*) also show that as $\kappa \to 0$ (long wave indicated by the red dot), the growth rate and phase speed of the exponential, as well as the PL modes, asymptote to the KH values provided by expression (3.1). The fastest growing mode for the exponential profile is indicated by the green dot in both figures. The red dot corresponds to a Fourier mode of wavelength ≈ 230 times the wavelength of the green dot. It is clear that both are long wavelength modes compared with the shear layer thickness ($\lambda/\Delta \approx 3.1 \times 10^4$ for the red dot and $\approx 1.4 \times 10^2$ for the green dot). A qualitative difference is apparent between these two, long wavelength modes: the fastest growing mode (green dot) of the exponential profile grows somewhat slower than the KH growth estimate of (3.1), travelling at a speed that is nearly twenty times the KH prediction; cf. figure 3(*b*). Interestingly, its growth rate and phase speed both agree quite well with that of the PL model ('$\cdot \times \cdot$' symbol).

Having established that the fastest growing mode of the exponential profile in the high-Froude-number (and infinite Bond number and low density ratio) limit has a growth rate and phase speed agreeing with the corresponding mode of the PL profile, it becomes necessary to inquire about the nature of this mode in the PL profile. For this, we recall a few essential stability properties of the PL profile. This base state of figure 2(*a*), by virtue of having a density interface (zero thickness) much smaller in thickness than the shear layer, admits the H instability (interaction between a vorticity and a density interface) as well as the KH instability (interaction between two vorticity interfaces; see Carpenter *et al.* (2011) and references therein). Under the Boussinesq approximation, depending on the choice of parameters on the Richardson number $J \equiv (1-\delta)g\Delta/(U_\infty^2(1+\delta))$ versus wavenumber (κ) space, the instability can be dominantly one of the two types or even of a mixed nature. As noted by Lawrence *et al.* (1991), the PL profile that we employ is an asymmetric profile, implying that the centre of its shear layer ($z = \Delta/2 > 0$; see figure 2*a*) does not coincide with the location of the density interface ($z = 0$). Indeed, the velocity profile of figure 2(*a*) may be recovered from that of Lawrence *et al.* (1991) by setting $u_2 = 0$ and their asymmetry parameter ϵ to unity (refer to figure 1 of Lawrence *et al.* 1991). Unlike symmetric profiles, for asymmetric profiles, the transition between the KH and H instability is not readily apparent on the $J - \kappa$ plane, as both modes have non-zero phase speeds; see Carpenter *et al.* (2010, § *B*, p. 9) and the related study by Barros & Choi (2011) for non-Boussinesq effects. Using wave resonance ideas reviewed in Carpenter *et al.* (2011), one can use the phase speed versus wavenumber plane to conclude if the dominant contribution comes from the KH (vorticity–vorticity resonance) or the H instability (vorticity–density resonance) for the fastest growing mode of figure 3(*a*). We defer this exercise to § 3.2.1 (the low-Froude-number limit), where we show that at low Froude number and low as well as moderately high density ratio, growing modes in the PL model arise due to resonance between a surface-gravity mode and a vorticity wave (i.e. the H instability dominates over the KH instability).

Figures 4(*a*) and 4(*b*) present the vertical variation of the (inviscid) Reynolds stress $-\overline{\rho uw}(z)$ and (twice) the perturbation kinetic energy $\overline{u^2 + w^2}(z)$ for both wavenumbers (green and red dots) of figure 3. In these (and subsequent figures) the Reynolds stress and perturbation kinetic energy have been normalised by their respective values at $z = 0$. The overbar indicates averaging along the horizontal coordinate over one wavelength, i.e.

$$\overline{uw}(z,t) \equiv \frac{1}{\lambda}\int_x^{x+\lambda} u(x,z,t)\, w(x,z,t)\, \mathrm{d}x. \tag{3.3}$$

Recall that the base-state vorticity ($DU_u(z)$ from (2.1)) is non-zero and positive in the approximate range $0 < z < \Delta$ in the upper fluid. This corresponds to $0 < z/z_c <$

https://doi.org/10.1017/jfm.2026.11588 Published online by Cambridge University Press

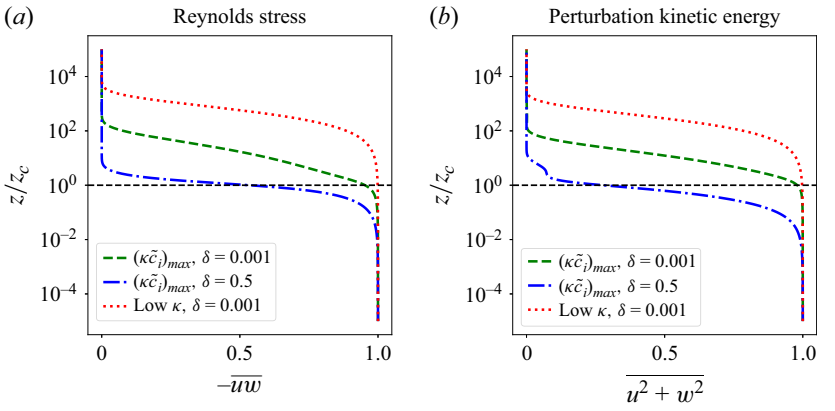


Figure 4. Vertical (z) profiles of (a) the Reynolds stress and (b) the perturbation kinetic energy in the upper fluid, normalised by their values at the location of the undisturbed interface at $z = 0$, for the exponential profile. Non-dimensional parameters: ($Bo \to \infty$, $Fr = 3194.8$). In panels (a,b) the red and green curves correspond to the low wavenumber and fastest growing modes from figure 3, respectively. The vertical coordinate z is scaled here by the coordinate z_c of the critical layer where the base velocity $U_u(z_c)$ matches the real part of the phase speed of an unstable mode, i.e. $c_r(k)$. The blue curve is for the fastest growing mode with $\delta = 0.5$.

$\Delta/z_c = 51.4$, (wavelength $\lambda/z_c \approx 7.2 \times 10^3$) for the green curves and $0 < z/z_c < \Delta/z_c = 832.2$, ($\lambda/z_c \approx 2 \times 10^7$) for the red curves, in both panels of figure 4. It is clear that the perturbation kinetic energy $(\overline{u^2 + w^2})(z)$ as well as the Reynolds stress $((-\overline{\rho uw})(z))$ becomes non-zero close to the onset of the shear layer for both modes. While the fastest growing mode (green curves) reaches its plateau very close to its maximum value at the critical layer ($z/z_c = 1$) in both panels, the KH mode (red) plateaus significantly before the critical layer is reached, i.e. $z/z_c \sim 100$. One may derive an equation for the rate of growth of perturbation kinetic energy, *viz.* $E_k(z) \equiv (1/2)\rho(\overline{u^2 + w^2})(z)$, which is (see Smyth & Peltier (1989), Equation (4))

$$\frac{\partial E_k(z)}{\partial t} = -(DU(z))\overline{\rho uw}(z) - D\overline{wp}(z). \tag{3.4}$$

In (3.4) the first term on the right-hand side is the rate of work done by the Reynolds stress and has the physical interpretation of a source term involving energy (per unit volume) extraction from the base state, when it is positive. The second term however, represents the (z) divergence of the flux of perturbation kinetic energy/volume and acts to redistribute the available perturbation kinetic energy (see discussion in Smyth & Peltier (1989), p. 3705). The vertical variation of Reynolds stress in figure 4(a) shows that, for the fastest growing mode (green curve), the dominant energy extraction from the base state occurs in the region between the critical layer and the interface, i.e. $0 < z/z_c < 1$. In contrast, for the low wavenumber KH mode (red curve), a significant proportion of the energy extracted from the base-state shear also occurs in the region where the shear commences $z \approx \Delta$ and up to the critical location, i.e. $z/z_c = 1$.

3.1.2. *Higher density ratio ($\delta < 1$)*

We now move towards a higher density ratio and the high-Froude-number regime. As discussed, the PL profile admits instabilities even for the unstratified case ($\delta = 1$) due to resonance between the vorticity interfaces at $z = 0$ and $z = \Delta$; see the Boussinesq approximation in Lawrence *et al.* (1991, Figure 3d) in the Boussinesq approximation). While the growth rates of the fastest growing mode in the exponential model agree reasonably well

https://doi.org/10.1017/jfm.2026.11588 Published online by Cambridge University Press

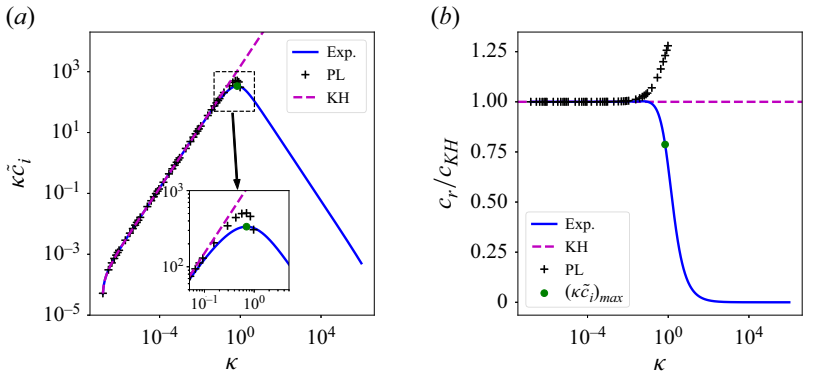


Figure 5. The infinite Bond ($Bo \to \infty$), high Froude ($Fr = 3194.38$) number and high density ratio ($\delta = 0.5$) case. (*a*) Growth rate ($\kappa\tilde{c}_i$) and (*b*) phase speed (c_r/c_{KH}) as a function of the non-dimensional wavenumber κ for the KH dispersion relation from (3.1) (pink dashed curve) for the exponential profile (solid blue curve) from (2.12) and for the PL profile from the dispersion relation in (3.2) ('+' symbols) for the base states of figures 1 and 2. The green dot indicates the fastest growing mode in both panels. The phase speeds of the PL and the exponential profile are markedly different.

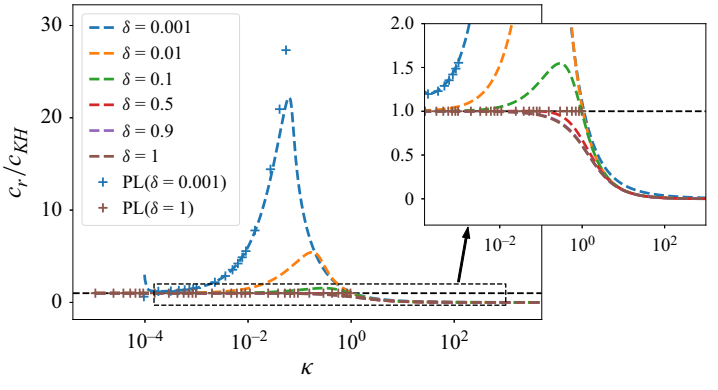


Figure 6. Variation of phase speed with wavenumber for varying density ratios. Here $Bo \to \infty$, $Fr = 3194.38$ for all cases. All dashed curves are for the exponential model of (2.1).

with the corresponding PL mode (figure 5*a*), the phase speed differs noticeably (figure 5*b*). The corresponding Reynolds stress and perturbation kinetic energy for the fastest growing mode are plotted in blue in both panels of figure 4. Note the appearance of a peak in the perturbation kinetic energy at the location where the shear layer commences, i.e. $\Delta/z_c \approx 3.29$, we have checked that no such peak is detected for the fastest growing mode at the air–water density ratio (green curves corresponding to $\delta = 0.001$ in figure 4). This change in the nature of the variation of c_r/c_{KH} with wavenumber κ for unstable wavenumbers as the density ratio is varied is seen both in the PL model and in the exponential model in figure 6, where a systematic increase of density ratio up to unity is reported.

3.2. *Infinite bond ($Bo \to \infty$) and low Froude number ($Fr \sim 1$)*

We next turn to the case of infinite Bond number, and moderately low Froude number, examining the effect of the variation of density ratio on the instability mechanism in the exponential profile. Before doing this, it is useful to digress and highlight the instability mechanisms in the PL profile of figure 2(*a*) within this parameter regime of interest

https://doi.org/10.1017/jfm.2026.11588 Published online by Cambridge University Press

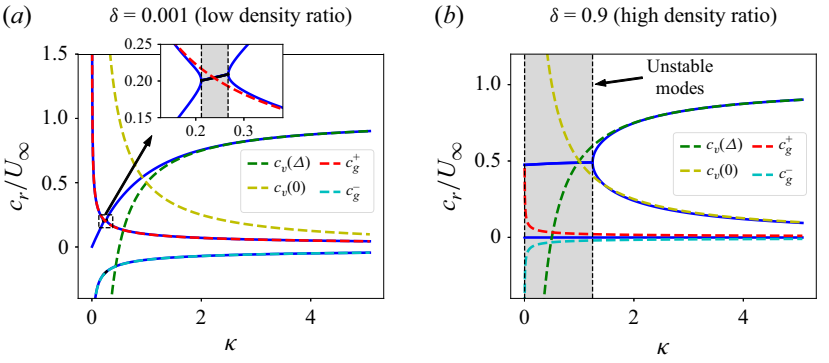


Figure 7. ($Bo \to \infty$, $Fr \approx 10$) The normalised phase speed (c_r/U_∞) variation with wavenumber κ for the isolated prograde ($c_v(0)$) and retrograde ($c_v(\Delta)$) vorticity modes as estimated using Carpenter *et al.* (2011, Equation 25) and isolated surface-gravity modes with $c_g^{+/-}$ (2.14*a*). The three solid blue curves are the roots of the dispersion relation given by (3.2). The grey shaded regions represent unstable wavenumbers. In the inset of panel (*a*), unstable wavenumbers are indicated as black solid curve. (*a*) At low $\delta = 0.001$, the instability is the result of resonance between the prograde gravity-capillary wave and the retrograde vorticity wave. (*b*) At higher $\delta = 0.9$, the instability is the result of resonance between the prograde and the retrograde vorticity waves. Consistent with the Howard semi-circle theorem (Morland & Saffman 1993), unstable wavenumbers have their phase speeds satisfying $0 < c_r/U_\infty < 1$ in both panels.

as a function of density ratio; these results will serve as reference for the exponential profile emphasising the role of background curvature. In this context, we note the study by Morland *et al.* (1991) who compared free surface waves subject to shear (only in lower layer with $\delta = 0$) generated by an exponentially decaying velocity profile (infinite depth) against those from a PL profile. The instability for their PL profile (Morland, Saffman & Yuen 1991) was shown to be a H-like instability, arising due to resonance (referred to as 'collision' in Morland *et al.* (1991)) between a retrograde capillary-gravity mode and a prograde vorticity mode. Here 'prograde' and 'retrograde' modes are defined (following Carpenter *et al.* (2011)) as those that travel leftward (negative velocity) or rightward (positive velocity), respectively, in a frame of reference that moves at the local background speed at the vorticity or density interface; see the explanation around equation (25) in Carpenter *et al.* (2011). We see in the next subsection that an analogous H instability occurs in our PL profile of figure 2(*a*) at a low density ratio and low Froude number.

3.2.1. *The instabilities in the PL profile at low Fr: density ratio (δ) variation*

Here, we interpret the instabilities admitted by the PL profile of figure 2(*a*) at a low Froude (infinite Bond) number and for a varying density ratio, employing wave resonance ideas reviewed in Carpenter *et al.* (2011). Figure 7(*a*) shows the phase speed versus wavenumber (refer to the inset for the narrow range of wavenumbers, which are unstable and shaded) for the PL profile at $\delta = 0.001$ and $Fr \approx 10$. The three solid blue lines in the figure are obtained from the numerical solution to the dispersion relation given by (3.2). Recall that the density interface at $z = 0$ (see figure 2*a*) supports stable prograde and retrograde surface-gravity waves in the absence of shear (labelled as c_g^+ (dashed red line) and c_g^- (dashed cyan line) in figure 7*a*). The vorticity interface when present alone at $z = \Delta$ and in the absence of stratification supports a stable retrograde vorticity wave ($c_v(\Delta)$, green dashed line in figure 7*a*). Similarly, the vorticity interface at $z = 0$ when present alone supports a stable prograde vorticity wave ($c_v(0)$, yellow dashed line); note that one of the blue curves computed from the numerical solution to (3.2) asymptotes to the green dashed line in figure 7(*a*). However, the other two blue curves from the numerical solution to (3.2)

https://doi.org/10.1017/jfm.2026.11588 Published online by Cambridge University Press

are indistinguishable from the two c_g modes, indicating the negligible effect of shear on the phase speed of these.

The inset in figure 7(a) makes it clear that the instability in the PL model (in this regime) arises due to resonance between the prograde gravity wave (c_g^+) at $z = 0$ and the slightly modified version of the retrograde vorticity wave at $z = \Delta$ (blue curve asymptotic to the green dashed line). Refer to the inset where that the coalescence of these aforementioned curves produces the band of unstable wavenumbers indicated by the shaded region; we conclude that these wavenumbers in figure 7(a) are H unstable following the definition of the H instability (Carpenter *et al.* 2011). In figure 7(b) a qualitatively different behaviour is seen at a much higher density ratio of $\delta = 0.9$ ($Fr \approx 10$). Now the band of unstable wavenumbers (hashed region) arise from resonance between the two vorticity waves at $z = 0$ and $z = \Delta$, as might be intuitively expected from a consideration of the PL configuration, excluding stratification, i.e. at $\delta = 1$. In figure 7(b), these wavenumbers are KH unstable, propagating nearly at the mean background speed $U_\infty/2$, consistent with (3.1). It is thus established that for a low Froude number, the PL model of figure 2(a) admits the H instability at a low density ratio, transitioning to the KH instability at a higher density ratio closer to unity. How does inclusion of background profile curvature affect this H instability? We answer this next.

3.2.2. *Low density ratio ($\delta \ll 1$) – instability in the exponential profile*

Having discussed the two instabilities in the PL profile, we now turn to studying the effect of background curvature at the low Froude number and low density ratio regime where the PL profile was studied in the previous subsection. Because of the presence of a critical location where the background profile curvature is non-zero, instead of the H instability we now expect to recover the classic Miles (1957), wind-wave instability, dominated by critical location dynamics. In this context, it is relevant to mention the recent study by Carpenter *et al.* (2017), which extends the wave interaction mechanism discussed in § 1, in the context of the KH and H instability, to the Miles instability as well. Interestingly, they show that the Miles critical layer instability (at the air–water density ratio) can be interpreted as resonance between a vortex sheet at the critical layer and a surface wave at the density interface.

We note that our choice of low $Fr \approx 4.8$ in this subsection is in the same ballpark range as Young & Wolfe (2014); see their figure 11 where their smallest Froude number of $\sim$1.4 corresponds to the air–water oceanic situation. In this parameter regime the fastest growing mode has features of a classic 'Miles mode' of instability (Miles 1957) dominated by the critical layer (Miles 1957; Young & Wolfe 2014; Kadam, Patibandla & Roy 2023); figure 8 presents data to support this. Unlike the high Froude cases studied previously, the fastest growing mode in the moderate Froude case (figure 8a) travels nearly at the surface-gravity wave speed, *viz.* c_g. Note that $c_g/c_{KH} = ((1-\delta^2)/\delta^2)^{1/2}\kappa^{-1/2}Fr^{-1} \gg 1$ for the air–water density ratio, as for the fast growing mode $\kappa = O_m(1)$ with $Fr = O_m(1)$; see figure 8(a). The fact that at sufficiently low δ, unstable, prograde modes travel nearly at the corresponding surface-gravity wave speed in still air/water is originally due to Miles (1957). This has been derived formally by several subsequent studies following Miles' procedure of expanding the eigenfunction and eigenvalue in the Rayleigh equation, employing a density ratio as a small perturbation parameter, e.g. see below equation (3.10) in Alexakis *et al.* (2002) or figure 3 in Young & Wolfe (2014) where capillarity has also been taken into account. In what follows, we illustrate several attributes of the fastest growing Miles mode and use these as reference to contrast the change observed, as the density ratio is increased significantly beyond that of air–water.

https://doi.org/10.1017/jfm.2026.11588 Published online by Cambridge University Press

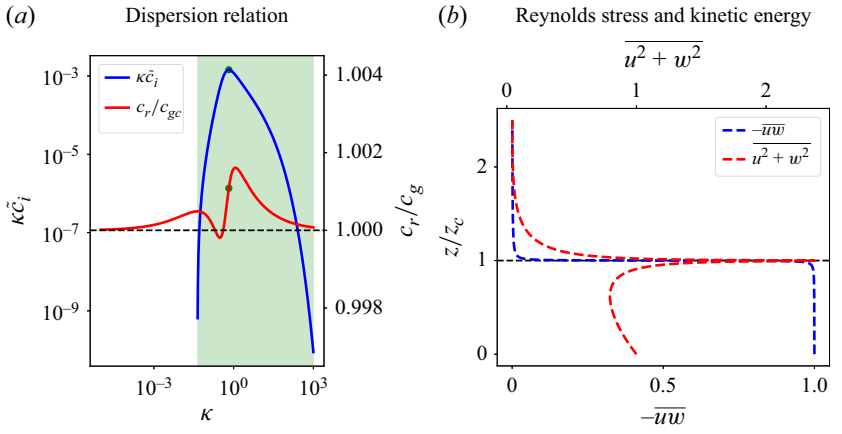


Figure 8. The infinite Bond ($Bo \to \infty$), low Froude ($Fr = 4.79$) number and low (air–water) density ratio ($\delta = 0.001$) case. (*a*) Growth rate ($\kappa\tilde{c}_i$) and phase speed (c_r/c_g) as a function of the wavenumber κ. The shaded region is that beyond which it is numerically challenging to detect growth, due to a very small growth rate ($< 10^{-12}$). (*b*) Vertical variation of Reynolds stress and perturbation kinetic energy for the fastest growing mode represented by dots in (*a*) with $\lambda/z_c \approx 32$.

Figure 8(*b*) presents the vertical variation of perturbation kinetic energy and the Reynolds stress for the fastest growing 'Miles mode' (dots in figure 8*a*). Note the classic near-discontinuous behaviour of the Reynolds stress at the critical location $z/z_c = 1$. This is consistent with Lin (1954) (their equation (3.10)) who showed, following Tollmien (1935), that the Reynolds stress $\tau(z) \equiv \overline{-\rho uw}$ across the critical location z_c (at which $D^2U_u < 0$ and $DU_u \neq 0$) jumps by the amount

$$\tau(z = z_c^+) - \tau(z = z_c^-) = \frac{\pi}{k}\left(\frac{D^2U_u}{|DU_u|}\right)_{z=z_c} \overline{\rho w_c^2} \tag{3.5}$$

for a singular neutral mode, i.e. a neutral solution to the Rayleigh equation for which there is a critical layer with $D^2U_u(z_c)$, $DU_u(z_c) \neq 0$; refer to Tollmien's inviscid solution in equations (22.25) and (22.26) in Drazin & Reid (2004) or around equation (2.7) in Stewartson (1981). In (3.5), w_c is the vertical perturbation velocity at the critical location z_c. Although figure 8(*b*) has been plotted for the fastest growing Miles mode (and not the neutral mode to which (3.5) applies), even for the fastest growing Miles mode $c_i/c_r \approx 0.001 \ll 1$, leading to the near-discontinuous behaviour seen in the Reynolds stress (see further discussion on this around (3.6)). In figure 8(*b*) the shear layer is between $0 < z/z_c < \Delta/z_c \approx 3.4$ and it is clear that the energy extraction (work done by the Reynolds stress term in (3.4)) from the base state occurs only within the thin region between the critical layer and the interface. We also contrast figure 8(*b*) (where $Fr \sim O(1)$) with its counterparts presented earlier in figure 4 ($Fr \gg 1$). Unlike in figure 8(*b*), sizable contributions to both perturbation kinetic energy and Reynolds stress in figure 4 were noted in the region between the start of the shear layer and the critical location ($1 < z/z_c < \Delta/z_c$).

Figure 9 shows the (real part) of the perturbation streamfunction for the fastest growing mode in figure 8(*a*). A clear bend in the streamfunction contours is visible at $z = z_c$ (figure 13(*a*) in Young & Wolfe (2014) notes the same behaviour), indicating the phase change in the perturbation streamfunction, characteristic of the critical layer. This in turn generates the phase change in perturbation pressure across $z/z_c = 1$, causing the

https://doi.org/10.1017/jfm.2026.11588 Published online by Cambridge University Press

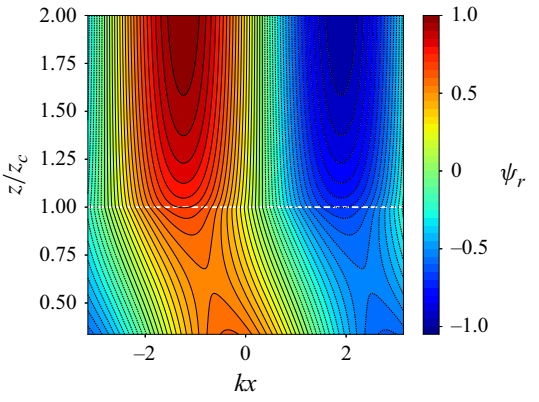


Figure 9. Real part of the perturbation streamfunction $\psi_u(x, z, t = 0)$ (2.3) for the fastest growing mode showing the tilt in the isocontours indicating a phase shift. The non-dimensional parameters are the same as in figure 8. The dotted white line is the critical location.

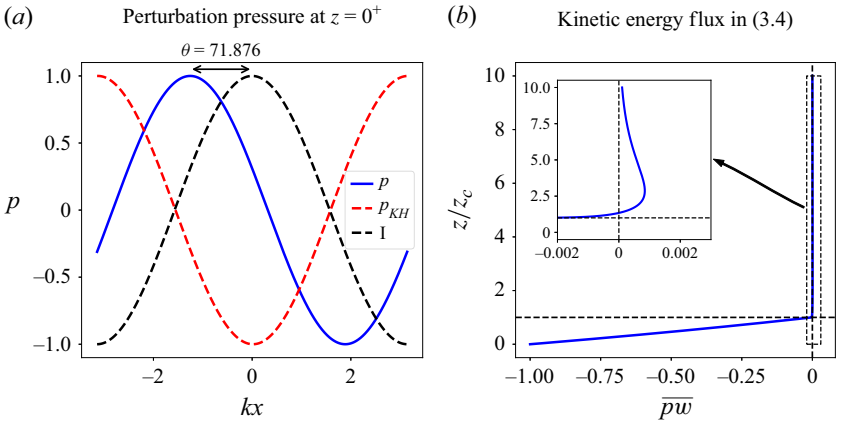


Figure 10. (*a*) Variation of perturbation pressure for the fastest growing mode at $z = 0^+$ with horizontal coordinate x in figure 8(*a*). Here $Fr = 4.79$, $\delta = 0.001$, $Bo \to \infty$. The dotted black line represents the real part of the perturbed interface given by η in (2.4). The blue curve corresponds to perturbation pressure for the fastest growing Miles mode in figure 8(*a*). The red dashed line represents the perturbation pressure $p(z = 0^+)$ obtained from the KH model of figure 2(*b*) for $\delta = 0.001$ and (in CGS units) $U_\infty = 1000$. (*b*) The vertical variation of the second term on the right-hand side of (3.4).

perturbation pressure (see (2.7) relating the streamfunction $\Psi(z)$ to perturbation pressure) to have a component in phase with $\partial\eta/\partial x$. As lucidly explained in Miles (1959), at the air–water density ratio the pressure component in-phase with $\partial\eta/\partial x$ is more efficient than the one in-phase with $-\eta$ in generating instability; this leads to a much lower threshold of instability for the critical wind speed when gravity and capillarity are both accounted for in the exponential model as compared with the corresponding discontinuous KH model (see figure 1 in Kadam *et al.* (2023)).

Figure 10(*a*) notes the variation of the perturbation pressure $p_u(x, z = 0^+, t = 0)$. If the perturbation pressure just above the interface (air side) were to be entirely in phase with $\partial\eta/\partial x$, the phase difference with η (black dashed curve in figure 10*a*) would be $\pi/2$, as for the Jeffrey model discussed earlier (see discussion around their equation (1.1) in Bonfils *et al.* (2022)). For the fastest growing Miles mode in figure 10(*a*), the phase angle ($\approx 72°$)

https://doi.org/10.1017/jfm.2026.11588 Published online by Cambridge University Press

is much closer to $\pi/2$ compared with the angle π of the KH model (red dashed curve) – we note in passing that the angle π for the KH model changes with increasing δ. Figure 10(b) notes the vertical variation of the kinetic energy flux (second term in (3.4)) for the fastest growing Miles mode, note the sign change in the flux around z_c, indicating that a thin layer centred around the critical layer redistributes the bulk of the generated perturbation kinetic energy towards the interface and a much smaller fraction away from it. In the budget for wave energy integrated vertically over the entire domain, the integration of this flux-divergence term in (3.4) equals the potential energy of the interface (purely gravitational in the current case); see Young & Wolfe (2014, Equation (3.2)).

We next turn to examining the effect of increase of density ratio (δ) on the fastest growing mode in the low-Froude-number regime of current interest. In order to rationalise the behaviour of the dispersion relation of (2.12), it is useful to compare the numerical solution to this against the approximation obtained in the low density ratio limit by expanding $\tilde{c}(\kappa;\,\delta)$ as $\tilde{c} = \tilde{c}_0(\kappa) + \delta\tilde{c}_1(\kappa) + \mathcal{O}(\delta^2)$ for fixed Froude and Bond numbers.

For the zero surface-tension limit relevant here, we use the expression upto $\mathcal{O}(\delta)$ obtained by Carpenter *et al.* (2017) (see equation (15) in their study). This, expressed in our notation is

$$\tilde{c} \approx \tilde{c}_0 + \delta\tilde{c}_1 = \tilde{c}_0 + \frac{\delta}{2\kappa}\left[Fr + \tilde{c}_0\left(\Xi\left(\tilde{c}_0,\,\kappa;\,Fr\right) - \kappa\right)\right], \tag{3.6}$$

with ($\tilde{c}_0 \neq Fr$)

$$\tilde{c}_0 \equiv \kappa^{-1/2},\;\; \Xi\left(\tilde{c}_0,\,\kappa;\,Fr\right) \equiv -\kappa + \left(\frac{1}{1+2\kappa}\right)\left(\frac{Fr}{Fr-\tilde{c}_0}\right) \frac{{}_2F_1\left(\alpha+1,\,\beta+1,\,\gamma+1;\,\dfrac{Fr}{Fr-\tilde{c}_0}\right)}{{}_2F_1\left(\alpha,\,\beta,\,\gamma;\,\dfrac{Fr}{Fr-\tilde{c}_0}\right)}, \tag{3.7}$$

the definitions of α, β and γ being available below (2.8). We remind the reader that the perturbative expansion (3.6) assumes that $\delta \to 0$, $Fr = \mathcal{O}(1)$, thus excluding the high Froude ($Fr \to \infty$) limit studied earlier.

Figures 11(a) and 11(b) compare the numerical solutions to the complete dispersion relation from (2.12) (solid lines) with the approximation in (3.6) (big and small dots). One notes the increase in growth rate beyond the linear dependence (for $\delta = 0.5$) on δ predicted by (3.6). Note from figure 11(b) that as δ is increased, the correction to the phase speed (Doppler shifting) compared with $\tilde{c}_g$ (in still air–water $\tilde{c}_0 \approx \tilde{c}_g$) for the fastest growing mode becomes significant. We assert that this increase in $\tilde{c}_r$ in figure 11(b) indicates a change in the nature of the instability for the fastest growing mode as $\delta \to 0.5$. To support this argument, we compare the growth rate ($\kappa\tilde{c}_i$) at $\delta = 0.5$ for the exponential model (solid red curve in figure 11a) with the PL model (dashed black line in figure 11a), noting the good agreement between the two around a region of wavenumbers close to the fastest growing mode; note also the match in the phase speed in figure 11(b), although there is evident a mismatch for wavenumbers centred around the fastest growing mode (dashed black curve and solid red curve). We noted in the last section that at a low Froude numbers and low density ratio, the instability in the PL model is the H instability. It is further shown in the supplementary material (§ 2) that the H instability persists until $\delta \approx 0.5$ at low Fr for the PL model (although KH contributions are also apparent; see figure 2(a) in the supplementary material). Given the good agreement seen in the growth rates between

https://doi.org/10.1017/jfm.2026.11588 Published online by Cambridge University Press

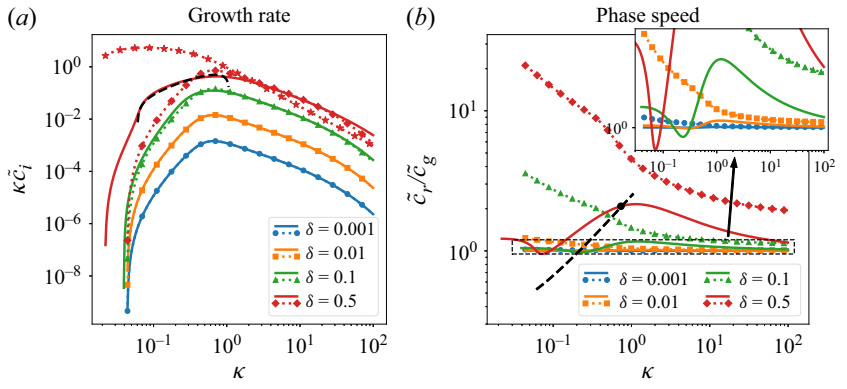


Figure 11. (*a*) Growth rate and (*b*) phase speed variation with κ for the exponential profile. Non-dimensional parameters: $Fr = 4.79$, $Bo \to \infty$. In both panels, solid lines are from the full dispersion relation in (2.12) while large and small dots are from the approximation (3.6). The dashed black line in both panels is from the PL model in figure 2(*a*) for the same non-dimensional parameters as above. The curve with stars and dots in panel (*a*) represents a comparison with formulae A31 in Appendix A of Alexakis *et al.* (2004*b*), valid for small Froude numbers, large wavenumbers and assuming that $c_i \ll c_r$. The black dot in panel (*b*) is for the fastest growing mode for the exponential model (solid red curve).

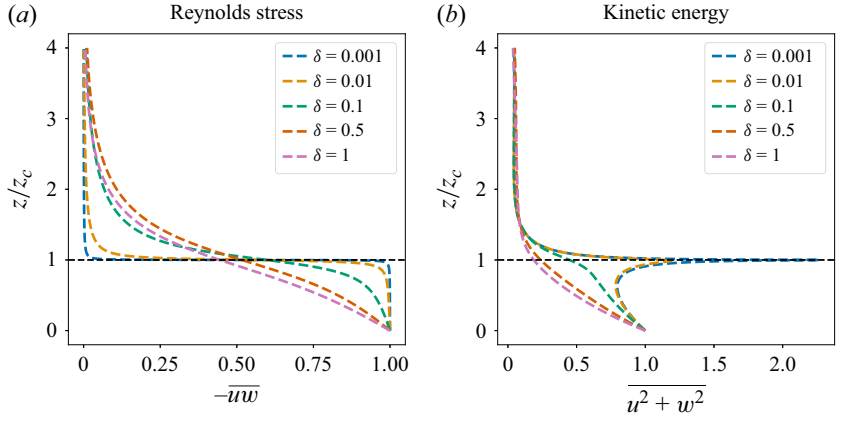


Figure 12. Vertical variation of (*a*) Reynolds stress and (*b*) perturbation kinetic energy for the fastest growing mode for every δ. The non-dimensional parameters are $Fr = 4.79$ and $Bo \to \infty$. In panel (*b*), note the transition from having a dominant peak at the critical layer to one only at the interface.

the PL and the exponential model in figure 11(*a*) at $\delta = 0.5$, we thus intuitively anticipate that the exponential model also admits the H instability around $\delta = 0.5$.

Our aforementioned assertion of a change from the Miles instability with increasing δ is further supported by the vertical variation in Reynolds stress (figure 12*a*) and perturbation kinetic energy (figure 12*b*) plotted for the fastest growing mode at every δ. Note in figure 12(*a*) the near-discontinuous jump for $\delta = 0.001$ at the critical layer noted earlier, giving way at $\delta = 0.5$, to a smooth transition through $z = z_c$ bereft of any distinguishing signature at this location; notice also that around $\delta = 0.5$, significant contributions appear to the Reynolds stress from the range $z/z_c > 1$ unlike the Miles case discussed earlier in figure 8(*b*). Why does the vertical variation of Reynolds stress in figure 12(*a*) for the fastest growing mode show a qualitative change as δ is increased? We address this question

https://doi.org/10.1017/jfm.2026.11588 Published online by Cambridge University Press

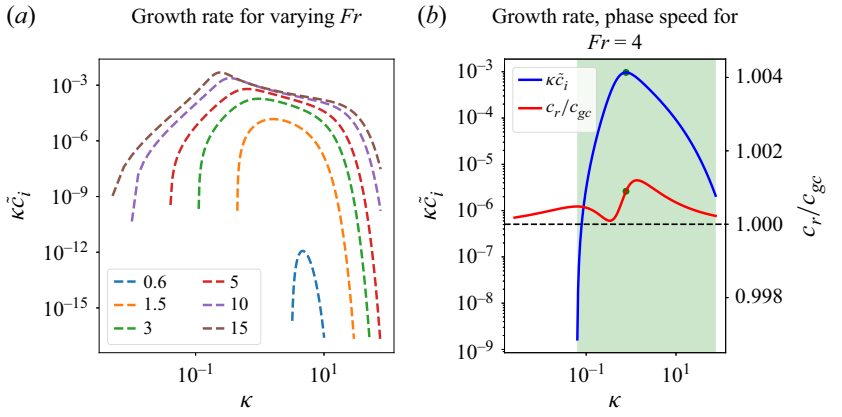


Figure 13. (*a*) Growth rate versus wavenumber for varying $Fr > Fr_c \approx 0.5$. For both panels, $\delta = 0.001$, $Bo = 87.813$. The shaded region indicates the range of wavenumbers, beyond which the growth rate is numerically very small. (*b*) Growth rate and phase speed for $Fr = 4$. The Froude number ($Fr = 4$) here has approximately the same value as in figure 8(*a*), which is for an infinite Bond number compared with $Bo = 87.813$ here.

in § 3.4; a noteworthy observation from this section is as δ increases from 0.001 to 0.5 in figure 12(*a*), the ratio c_i/c_r (for the fastest mode) increases from ≈ 0.001 to ≈ 0.42.

3.3. *Effect of capillarity*

We discuss the effect of capillarity in this section, restricting ourselves to the low-Froude-number regime where interesting transitions were recorded. As remarked earlier, the fastest growing mode studied so far are long waves (compared with the shear layer thickness as well as the air–water capillary length) and, thus, have subdominant contribution from surface tension. For consistency, we only present high-Bond-number results here ($Bo = \mathcal{O}_m(88)$) relevant to geophysical and astrophysical situations. A discussion of low-Bond-number instabilities is eschewed because these can involve shorter waves where the viscous contribution to Reynolds stresses as well as the Tollmien–Schlichting instability can become important (Miles 1962). In addition, for shorter wavelengths, one also expects the inviscid rippling instability (Stern 1973; Morland, Saffman & Yuen 1991; Shrira 1993; Young & Wolfe 2014; Kadam, Patibandla & Roy 2023) when shear is also included in the water layer, as discussed earlier for Morland *et al.* (1991); the growth rates for this can be significantly more than that of the longer wavelength modes, especially at a low density ratio. An important difference here, compared with the infinite-Bond-number case is the existence of a critical Froude number $Fr_c > 0$ for instability. This is easily rationalised at $\delta \ll 1$. Recall that prograde, capillary-gravity waves propagating at the interface of still water/air (which are destabilised by shear in the upper fluid) have a non-zero, minimum phase speed (unlike the case of surface-gravity modes), thereby leading to a critical Froude number based on this minimum speed.

Figure 13(*a*) presents the growth-rate curves for varying Froude numbers at a low density ratio ($\delta = 0.001$). We note that $Fr_c \approx 0.5$ and the case with $Fr = 0.6$ in the figure 13(*a*), is very close to the instability onset. The $Fr = 4$ case (figure 13*b*) shows that the fastest growing mode in this case travels at almost c_{gc}. Examination of the Reynolds stress and perturbation kinetic energy for $Fr = 4$ in figures 14(*a*) and 14(*b*) establish that these correspond to a classic Miles mode with distinct (near) discontinuities and peaks, respectively, at z_c. Note the interesting behaviour of the fastest growing mode for $Fr = 0.6$

https://doi.org/10.1017/jfm.2026.11588 Published online by Cambridge University Press

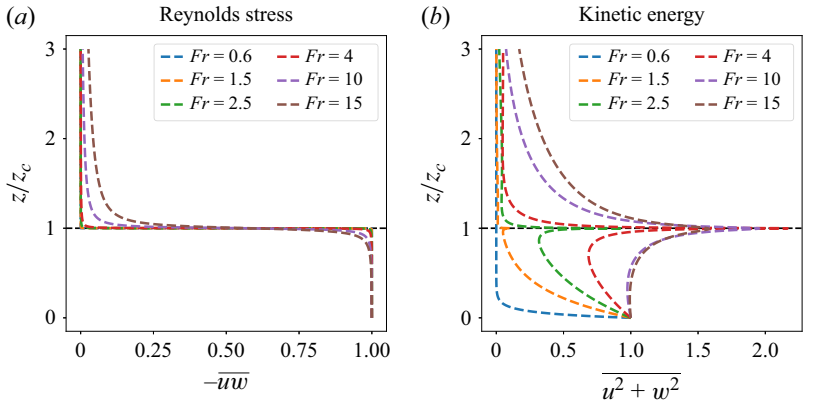


Figure 14. (*a*) Reynolds stress and (*b*) kinetic energy variation for fastest growing mode. Here $\delta = 0.001$, $Bo = 87.81$. In panel (*b*), note the non-monotonic behaviour of the peak at the critical layer with increasing Fr.

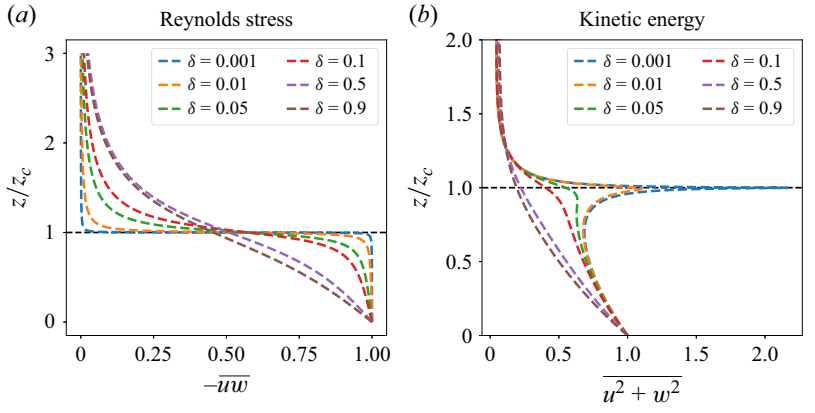


Figure 15. (*a*) Vertical variation of Reynolds stress and (*b*) kinetic energy for the fastest growing mode. Here $Fr = 4$, $Bo = 87.81$. In panel (*b*), note the transition from having a dominant peak at the critical layer to one at the interface, with increasing δ.

in these figures. There is a sharp near discontinuity at z_c (cf. figure 14*a*) for $\tau \equiv -\overline{\rho uw}$ but no corresponding signature at z_c in figure 14(*b*) for the kinetic energy. To conclude this section, figures 15(*a*) and 15(*b*) note the z variation of the Reynolds stress and perturbation kinetic energy (for the fastest growing mode in each case) with increasing density ratio; similar to figure 12 a clear change in the nature of variation of both metrics at $z/z_c = 1$ is observed.

3.4. *Why does the Reynolds stress become continuous at $z = z_c$ with increasing δ?*

We return to the question: Why does the Reynolds stress for the fastest growing mode show qualitative change with increasing δ? This behaviour is observed both in figure 12(*a*) (infinite Bond number) and in figure 15(*a*) ($Bo = 87.81$). It turns out that this can be understood from Lin's relation for the vertical variation of Reynolds stress $\tau(z)$ for an unstable mode with phase speed $c = c_r + ic_i$. Using background velocity as the

https://doi.org/10.1017/jfm.2026.11588 Published online by Cambridge University Press

independent variable (in place of z) this is

$$\frac{\mathrm{d}\tau}{\mathrm{d}U_u} = F(U_u)\left[\frac{c_i}{\left(U_u(z)-c_r\right)^2+c_i^2}\right], \tag{3.8}$$

where $F(U_u(z)) \equiv (1/k)(\mathrm{d}Z/\mathrm{d}U_u)\overline{\rho_u w^2(z)}$, $Z(z) \equiv DU_u$. For our exponential profile (2.1), DU_u can be rewritten in terms of U_u as

$$Z \equiv DU_u = \frac{U_\infty}{\Delta}\left[1-\frac{U_u}{U_\infty}\right]. \tag{3.9}$$

Using (3.9) in (3.8) simplifies to the following non-dimensional form:

$$-\left(\frac{1}{\rho_u \overline{w^2(z)}}\right)\left(\frac{\mathrm{d}\tau}{\mathrm{d}\tilde{U}_u}\right) = \frac{1}{\kappa}\left[\frac{\tilde{c}_i}{\left(\tilde{U}_u(z)-\tilde{c}_r\right)^2+\tilde{c}_i^2}\right]. \tag{3.10}$$

Here $\tilde{U}_u \equiv U_u/\sqrt{g\Delta}$. Importantly, even for the fastest growing Miles mode in figure 8, $c_i/c_r \ll 1$. Now using the observation that $\lim_{y\to 0}(1/\pi)[y/((x-x_0)^2+y^2)] \to \delta(x-x_0)$ (Lin (1954)), $\delta(x)$ being the Dirac delta function, we see that the quantity inside the square bracket in expression (3.10) for the fastest growing Miles mode has a near delta function behaviour and this generates the jump in the Reynolds stress in figure 8(*b*).

To visualise this, in figure 16(*a*) we plot the right-hand side of (3.10) as a function of the vertical coordinate (z) for the fastest growing mode in each case. As expected, the low Froude number ($Fr = 4$) and low density ratio ($\delta = 0.001$) has the signature of a Dirac delta function (blue dashed curve) leading to the jump behaviour of τ in figure 15(*a*). For the dashed green and red curves in figure 16(*a*), notice the widening as the ratio c_i/c_r increases significantly. For $\delta = 0.5$ (red curve with $c_i/c_r = 0.37$), a large fraction of the area under the curve comes from $z/z_c > 1$ with a smaller contribution from $z/z_c < 1$. This generates the observed smooth behaviour of τ through z_c in figure 15(*a*). Figure 16(*b*) justifies the transition seen with increasing density ratio from a slightly different viewpoint. Recall that Tollmien's inviscid solutions have a logarithmic singularity when the curvature at the critical location is finite (with $(DU_u)_c \neq 0$). Figure 16(*b*) computes the phase shift in such a term in a small region around $z/\mathrm{Re}(z_c) = 1$ (z_c is a complex number with $\mathrm{Im}(z_c) > 0$, and is computed for the fastest growing mode using $U_u(z_c) = c(k)$) with $c(k)$ being complex for the fastest growing mode. It is seen that a qualitative change occurs with increasing δ, *viz.* the abrupt jump in phase seen at $z/\mathrm{Re}(z_c)$ for the argument of the logarithmic term gives way to a smooth variation in figure 16(*b*). These aforementioned arguments pinpoint the source of the differences seen in the vertical variation of $\tau(z)$ between the low and high density ratio cases.

3.5. *Distinguishing between the H and KH instability for asymmetric profiles*

Given the good comparison between the growth rates at $\delta = 0.5$ of the PL profile and the exponential profile in figure 11(*a*), we hypothesise that at low Froude and high Bond numbers, the nature of the fastest growing mode in the exponential profile undergoes a transition – it changes from being dominated by the critical location for $\delta \ll 1$ to the H instability for $\delta \approx 0.5$ and eventually the KH instability at even larger δ. We emphasise that the KH to H transition seen clearly in the PL model occurs smoothly, in particular at $\delta = 0.5$ there seems to be contributions from both (see § 2 of the supplementary material). For the asymmetric, exponential background profile of figure 1, the vertical variation of the perturbation kinetic energy and the Reynolds stress do not show any qualitative change

https://doi.org/10.1017/jfm.2026.11588 Published online by Cambridge University Press

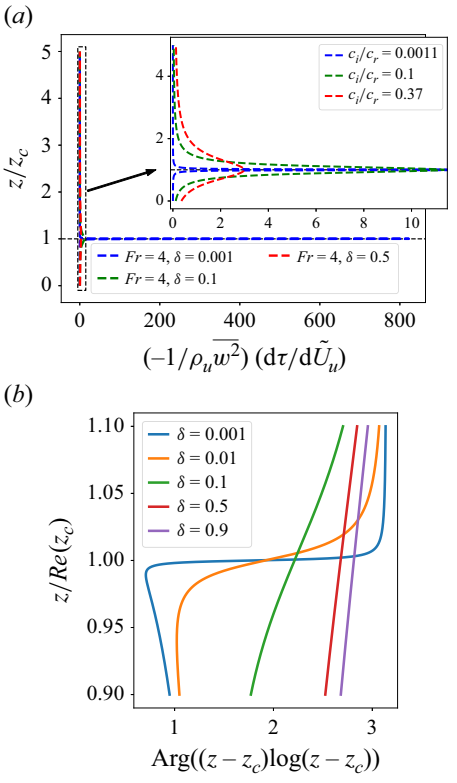


Figure 16. (*a*) Vertical variation of the right-hand side of (3.10) for the exponential profile for different density ratios. In each case, the fastest growing mode has been chosen. (*b*) Change in the phase of $(z - z_c)\log(z - z_c)$. This term appears in Tollmien's singular inviscid solution; see expressions (22.25) and (22.26) in Drazin & Reid (2004). For (*b*), $Fr = 4$, $Bo = 87.81$.

as δ is changed from 0.5 to 0.9, this may be ascertained from figures 15(*a*) and 15(*b*). This lack of distinction however is not indicative; even for symmetric curved background profiles, where the KH and H instability can be distinguished clearly based on phase speed, the corresponding Reynolds stress and the perturbation kinetic energy do not show qualitative differences in their vertical distribution. Smyth & Peltier (1989) comment on this in the first paragraph on p. 9 (note that the word inside the bracket has been added by us), 'the two (Holmboe) modes illustrated in figures ... are qualitatively very similar to KH modes...', emphasising the challenge of distinction between the two based on these metrics. One may, for example, use the diagnostic proposed in Carpenter *et al.* (2010) to partition the growth rate from the exponential profile into a H and a KH contribution; see their figure 9. We do not do this here, instead taking up numerical simulations of the incompressible, Euler's equations with surface tension and gravity; in the nonlinear regime captured through these simulations, clear differences are seen to emerge with increasing density ratio. These simulations clearly distinguish between the H and KH instability, as described next.

4. Numerical simulations – linear and nonlinear regime

In this section we present results from numerical simulations obtained by solving the incompressible, Euler's equations using the open-source code Basilisk (Popinet &

https://doi.org/10.1017/jfm.2026.11588 Published online by Cambridge University Press

Collaborators 2013–2025). We restrict ourselves to the low-Froude-number and high-Bond-number regime discussed earlier. To be consistent with the inviscid stability model discussed so far, we solve the incompressible Euler's equations with gravity and surface tension, in Basilisk, with an interface separating two fluids. The equations that are solved read as

$$\nabla . \boldsymbol{u} = 0, \tag{4.1a}$$

$$\frac{\partial \boldsymbol{u}}{\partial t} + \nabla . (\boldsymbol{u} \otimes \boldsymbol{u}) = -\frac{\nabla p}{\rho} + g + \frac{T}{\rho} \kappa \delta_s \boldsymbol{n}, \tag{4.1b}$$

$$\frac{\partial f}{\partial t} + \nabla . (f \boldsymbol{u}) = 0, \tag{4.1c}$$

where $\boldsymbol{u}$, p, κ, T and f are the velocity field, pressure field, interface curvature, surface tension and the volume-fraction field, respectively. The velocity field is $\boldsymbol{u} = (u, w)$, where u and w are horizontal and vertical components, respectively. Basilisk implements the volume-of-fluid algorithm in a one fluid formulation for reconstruction and advection of the interface separating the two fluids. This is done along with time marching of the accompanying velocity and pressure fields. A volume-fraction field $f(x, z, t)$ is defined that takes values $\in [0, 1]$. Specifically, in all computational cells containing only the upper or lower fluid, f takes the value 0 or 1. Thus, by definition the interface is present in those cells where $0 < f < 1$, the value representing the fraction of the cell that is occupied by one of the two fluids. Given an f field at any time instant, a reconstruction algorithm computes the interface using a PL approximation for each computational cell where $0 < f < 1$. The f field is advanced in time employing a discrete version of (4.1*c*); volume fluxes through cell walls being computed geometrically ensuring high accuracy of volume conservation; see Tryggvason *et al.* (2011) and references therein. The density and viscosity fields are computed as a weighted average of their respective values in the two phases, employing the local value of f as the weight.

It is important to note that the volume-of-fluid algorithm constructs a sharp representation of the interface. This representation is not just for visualisation, but is also explicitly employed to estimate the volume fluxes for each computational cell, while time stepping (4.1*c*). Surface tension is incorporated as a body force into the momentum equations and curvature is computed using a generalised, height-function algorithm (see § 5 in Popinet & Collaborators 2013–2025). The code has been benchmarked extensively, particularly at high Reynolds numbers including inviscid test cases (Popinet 2003; Kayal *et al.* 2025). We have, in particular, extensively employed the adaptive grid feature of this code in our current simulations. The criteria for adaptivity is based on changes to the volume-fraction field f, curvature κ and the velocity field, when subject to local grid refinement. The computational domain length has been chosen to match the wavelength λ of the fastest growing mode, obtained from theory. The smallest local grid size is (domain size)$/2^{13} = \lambda/2^{13}$. This level of adaptivity is referred to as 2^{13}, for example, in figure 19(*a*) and similarly in other figures. In some of the simulation results that follow, qualitative features are observed to remain unchanged under grid refinement, although quantitative changes are apparent in certain cases. A sample simulation file for the simulation reported in figure 20 is also provided (Kumar 2025).

Figure 17(*a*) depicts the simulation domain along with boundary conditions while figure 17(*c*) shows a sample adaptive grid employed. The initial conditions in our simulations are obtained from linear theory presented in § 2 (figure 17*b*). In both upper and lower fluids, we initialise the velocity field using a velocity field represented as base state (2.1) plus perturbation (2.3). The perturbation field is obtained from the analytically

https://doi.org/10.1017/jfm.2026.11588 Published online by Cambridge University Press

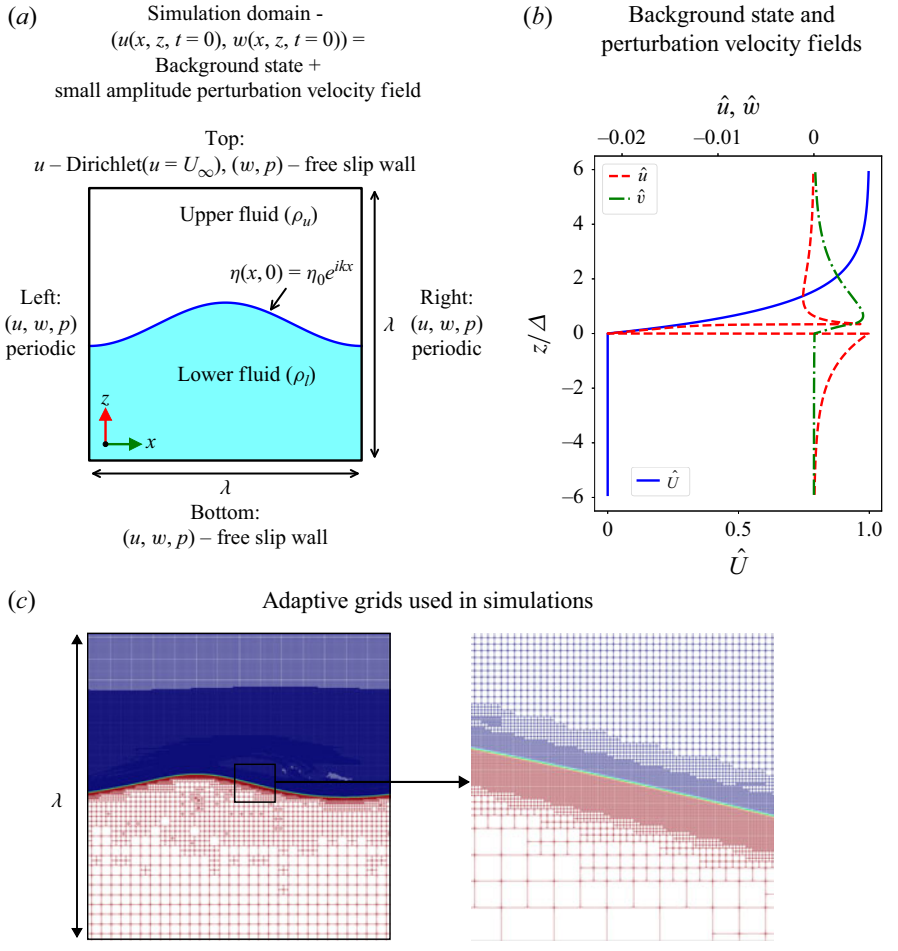


Figure 17. (*a*) A schematic of the computational domain along with boundary conditions implemented. (*b*) Vertical variation of fastest growing eigenmodes and background shear. A superposition of background shear with the fastest eigenmode with a small amplitude is used as the initial velocity field in all simulations. Here $(\hat{U}, \hat{u}, \hat{w}) \equiv (U/U_\infty, u/U_\infty, w/U_\infty)$. (*c*) Sample adaptive grid.

computed eigenfunctions in (2.11). Note that there is only one free parameter in our linear theory, *viz.* the value of η_0. The value of this is chosen such that the steepness $k\eta_0 = 0.02$ for all simulations, consistent with the linear theory assumed (small steepness). The interface is initialised using (2.4), employing the fastest growing wavenumber in each case, as computed from the dispersion relation in (2.12) for a Fourier mode travelling rightwards.

Figure 18(*a*) shows simulations for the case for $Fr = 4$, $Bo = 87.81$ and $\delta = 0.01$. The dimensional parameters for figure 18(*a*) are $U_\infty = 199.57$ cm s^{-1}, $\Delta = 2.54$ cm, $\rho_l = 1$ gm cm^{-3} and $\rho_l = 0.01$ gm cm^{-3}. For these parameters, the fastest growing mode in the exponential profile has wavelength ≈ 20.9 cm. We have seen earlier in figure 15(*a*) that the Reynolds stress vertical distribution with a sharp jump at the critical location is nearly identical for $\delta = 0.001$ (air–water) as well as $\delta = 0.01$, indicative of the critical location dominating the instability. In figure 18(*a*) we present the evolution of the interface from theory and simulations for this Miles regime. Note that time is measured in units of the duration (τ) taken for the wave to travel its wavelength; notice the slow growth in

https://doi.org/10.1017/jfm.2026.11588 Published online by Cambridge University Press

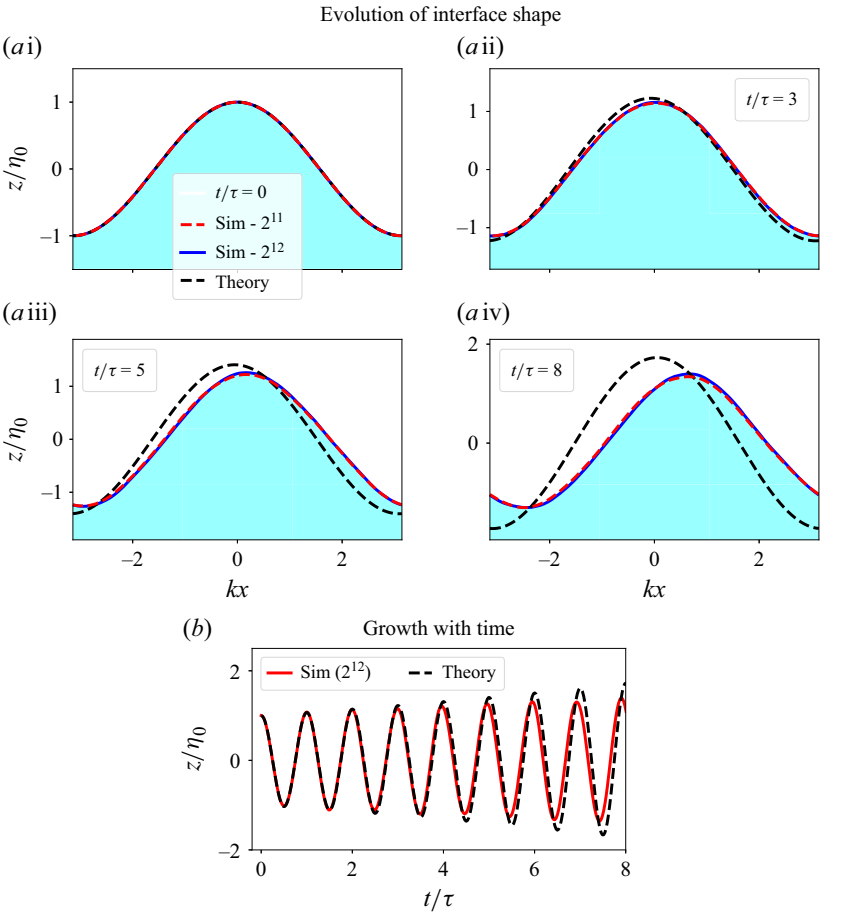


Figure 18. Panels (a i–a iv) compare the interface shape from theory and simulations. Non-dimensional parameters: $Bo = 87.81$, $Fr = 4$, $\delta = 0.01$ and $\Delta/\lambda = 0.12$ (rounded to two decimal places). (b) The time signal obtained by tracking interface displacement at $x = 0$ (horizontal midpoint of the domain). Here τ is the time taken for a Fourier mode to travel one wavelength.

figure 18(b). As the wave amplitude significantly exceeds its initial value, a mismatch with linear theory is apparent by $t/\tau = 5$ (five wave periods). We note that simulations for the air–water density ratio ($\delta = 0.001$) were also attempted; however, due to the extremely small growth rate, long simulations are necessary. Computational inaccuracies in such long runs prevented detection of any exponential growth and, thus, are not reported here. Figure 18 is the smallest density ratio ($\delta = 0.01$) where we were able to detect growth and compare against linear theory, while being in the critical layer dominated regime. Figure 18(b) reports the interface displacement at the centre of the domain and a slow exponential growth along with a reasonably good match with theory. Note that simulations were carried out at three adaptive resolutions: 2^{11}, for example, represents the upper limit of the number of grid points along each direction. A reasonably good grid convergence is apparent in figure 18(a).

Figure 19 is at the same Froude number as figure 18 but for a density ratio one hundred times that of air–water. We recall that even at these elevated values of δ, the Reynolds stress for the fastest growing mode in figure 15(a) retains a strong signature at the critical layer similar to the Miles instability for air–water. An interesting phenomena is apparent

https://doi.org/10.1017/jfm.2026.11588 Published online by Cambridge University Press

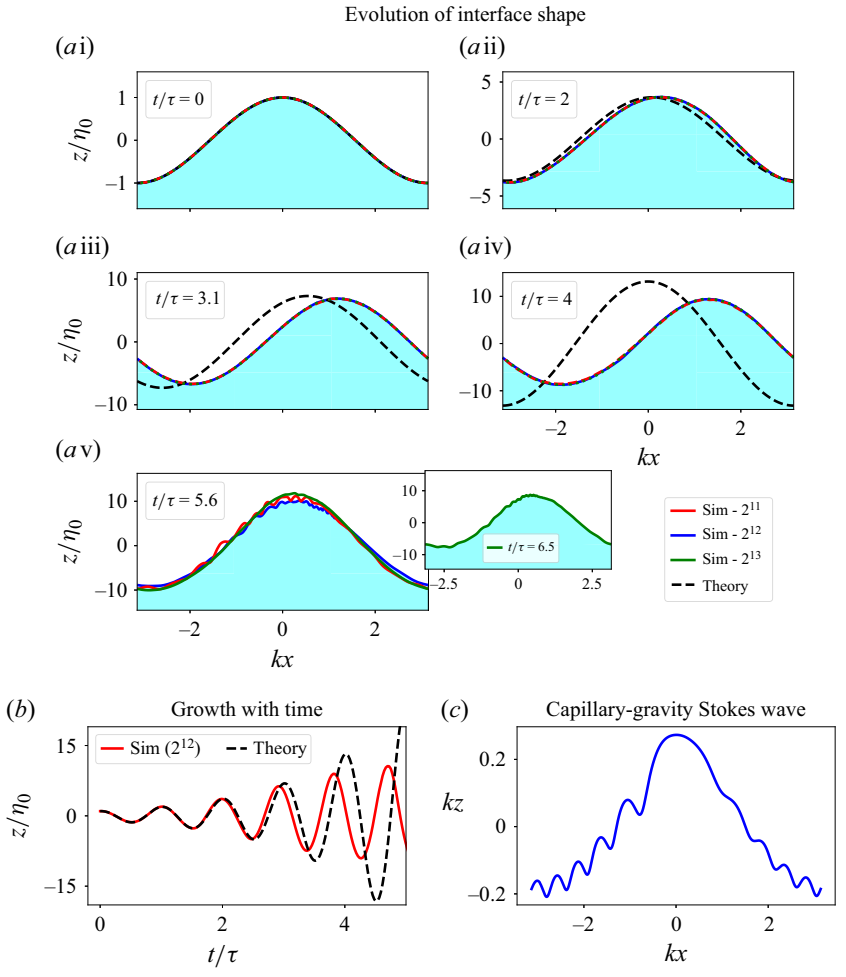


Figure 19. Panels (*a* i)–(*a* v) compare the interface shape from theory and simulations. Non-dimensional parameters: $Bo = 87.81$, $Fr = 4$, $\delta = 0.1$ and $\Delta/\lambda = 0.12$ (rounded to two decimal places). (*b*) Growth with time at $x = 0$. Notice the mismatch at larger time. (*c*) A finite-amplitude, capillary-gravity Stokes wave containing finer-scale ripples comoving with the wave. The shape is computed by solving the nonlinear, potential flow equations including gravity and surface tension following Shelton *et al.* (2025). For this nonlinear wave which is obtained by evolving the gravity-capillary Stokes wave in time, the initial steepness is 0.24, $Fr \equiv c_p/\sqrt{g\lambda} = 0.4389$ and $Bo \equiv \rho g \lambda^2/T = 384.615$, with $\delta = 0$ (no upper fluid). The shape of the wave as depicted here is obtained by propagating the initial Stokes wave and taking a snapshot at $t/\tau_S = 2$. Here λ, c_p and τ_S represent the wavelength, nonlinear phase speed and the time taken to travel one wavelength respectively for the capillary-gravity Stokes wave.

at $t/\tau = 5.6$; see the inset in figure 19(*a* v). A series of ripples developed on the backward face of the parent wave – some grid sensitivity is noted in their wavelengths. The inset to this subpanel describes the interface at a slightly later time $t/\tau = 6.5$ where the ripples are more clearly seen. These are reminiscent of ripples on capillary-gravity Stokes waves; see figure 2 in Hung & Tsai (2009) for the vortical structure of such ripples. For comparison, we have provided in panel (*c*), an irrotational, left to right propagating Stokes wave ($Bo = 384.615$, $Fr = 0.4389$), computed in the limit of $\delta \to 0$ with gravity and surface tension. This is a nonlinear, travelling wave solution to the potential flow equations and qualitatively similar structures are seen on the Stokes wave with a marked asymmetry

https://doi.org/10.1017/jfm.2026.11588 Published online by Cambridge University Press

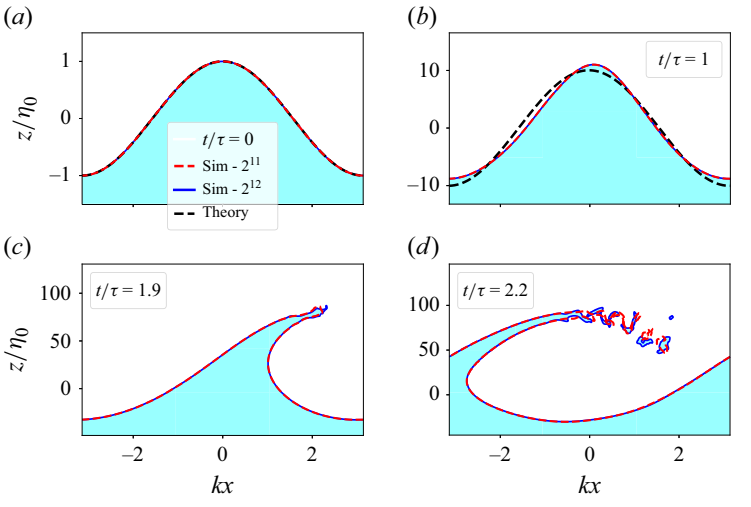


Figure 20. (*a*,*b*) Comparison of the interface shape with linear theory. (*c*,*d*) Finite-amplitude regime with H-like waves emitting spume-like droplets (Deike 2022) from the tip. Here $Bo = 87.81$, $Fr = 4$, $\delta = 0.5$.

between the forward and the backward face. Qualitative similarities may be seen between panel (*c*) and the inset in panel (*a* v) of figure 19. We have also compared numerical simulations for $\delta = 0.01$ (figure 18) and for $\delta = 0.1$ (figure 19) in the nonlinear regime upto the same value of $t/\tau_G \approx 3.5$ (data not shown here). Here $\tau_G \equiv (kc_i)^{-1}$ is the time scale of the growth of the instability (which depends on the density ratio) and is distinct from $\tau = 2\pi/(kc_r)$ (as is done in figures 18 and 19). We observe that the finite-amplitude wave for $\delta = 0.01$ has a far smaller steepness and exhibits tiny, ripple-like structures on its surface, compared with that for $\delta = 0.1$ where the finite-amplitude wave is significantly steeper (slope) and displays larger-amplitude ripples (upto grid precision).

As anticipated, a clear signature of differences in the nonlinear regime is seen between figures 20 and 21, as density is increased from $\delta = 0.5$ to $\delta = 0.9$, respectively. These differences are further seen readily in the collage of images provided in figure 22, all of them approximately at the same value of t/τ. One notes transitions in the nonlinear regime around $\delta \approx 0.3$ and $\delta \approx 0.7$. In figure 20 we particularly note the formation of a cusp-like structure at the crest that emits spume droplets (panel *d*) (Deike 2022); we treat this as a signature of the H instability. Compare figure 20(*d*) with the shape of the interface extracted from Lawrence *et al.* (1998) in figure 23(*a*) that is an asymmetric H instability. With a further increase in density ratio $\delta = 0.9$, we recover the classic KH spirals in figure 21(*d*), comparing this to figure 23(*b*), symptomatic of the asymmetric KH instability. Figures 20 and 21, as well as the collage of images in figure 22, thus show clear evidence that the nonlinear deformation regime is quite different for $\delta = 0.5$ compared with $\delta = 0.9$. While the former bears similarity to the asymmetric H instability of Lawrence *et al.* (1998) in figure 23, the latter is very much the asymmetric KH instability in the same figure. We thus validate our hypothesis that the fastest growing mode in the exponential profile indeed undergoes a transition from the Miles to the H instability and further to the KH instability, as the density ratio is increased.

In order to establish the qualitative validity of these inviscid simulations, we have also compared these against viscous simulations employing a realistic value for the viscosity of the fluids, at the density ratios of interest. To account for viscosity, the viscous term

https://doi.org/10.1017/jfm.2026.11588 Published online by Cambridge University Press

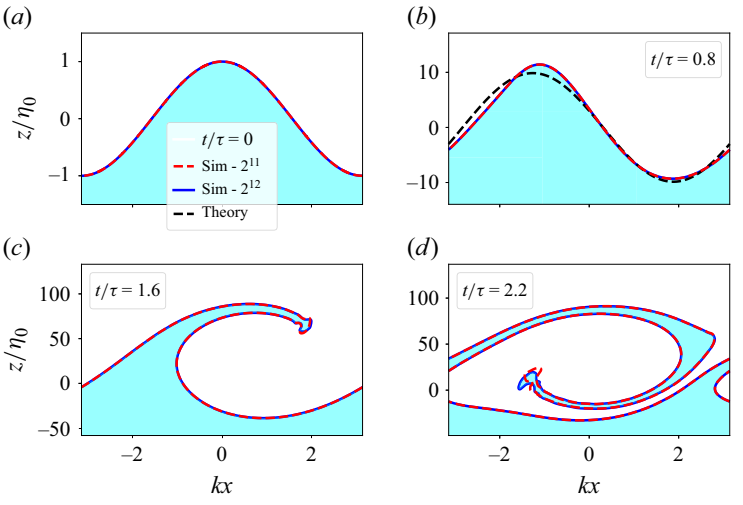


Figure 21. (*a*,*b*) Comparison of the interface shape with linear theory. (*c*,*d*) Finite-amplitude regime, note the formation of classic KH spirals in the last two panels. Here $Bo = 87.81$, $Fr = 4$, $\delta = 0.9$.

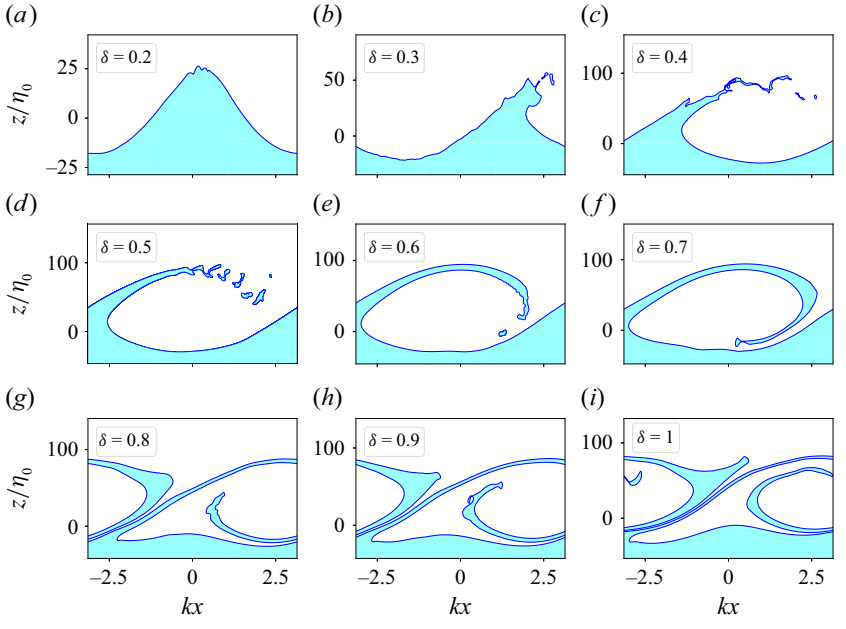


Figure 22. Results are shown for (*a*) $t/\tau = 2.863$, $\Delta/\lambda = 0.12$ (rounded to two decimal places); (*b*) $t/\tau = 2.897$, $\Delta/\lambda = 0.12$; (*c*) $t/\tau = 2.434$, $\Delta/\lambda = 0.12$; (*d*) $t/\tau = 2.278$, $\Delta/\lambda = 0.12$; (*e*) $t/\tau = 2.237$, $\Delta/\lambda = 0.12$; (*f*) $t/\tau = 2.270$, $\Delta/\lambda = 0.12$; (*g*) $t/\tau = 2.530$, $\Delta/\lambda = 0.13$; (*h*) $t/\tau = 2.489$, $\Delta/\lambda = 0.13$; (*i*) $t/\tau = 2.573$, $\Delta/\lambda = 0.13$. Non-dimensional parameters: $Bo = 87.81$, $Fr = 4$. The final set of images at δ close to unity bear remarkable similarity to the experimental images in figure 14.3 of Cushman-Roisin & Beckers (2011). We thank an anonymous referee for pointing us to these images.

$\nu\boldsymbol{\nabla}^2\boldsymbol{u}$ is added to the right-hand side of (4.1*b*). This addition converts the system described by (4.1) into the two-dimensional, Navier–Stokes equations, where ν is the kinematic viscosity. Two fluid combinations (water and perfluorodecalin) with a density ratio of 0.5 and fresh water and brine with a density ratio of 0.9 are considered. We emphasise

https://doi.org/10.1017/jfm.2026.11588 Published online by Cambridge University Press

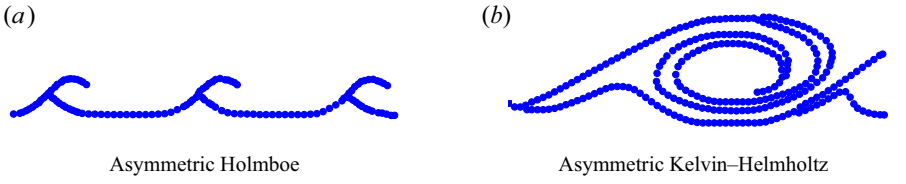


Figure 23. Data extracted from figure 9 of Lawrence *et al.* (1998). Compare panels (*a*) (asymmetric H) and (*b*) (asymmetric KH) of this figure with panel (*d*) of figures 20 and 21, respectively.

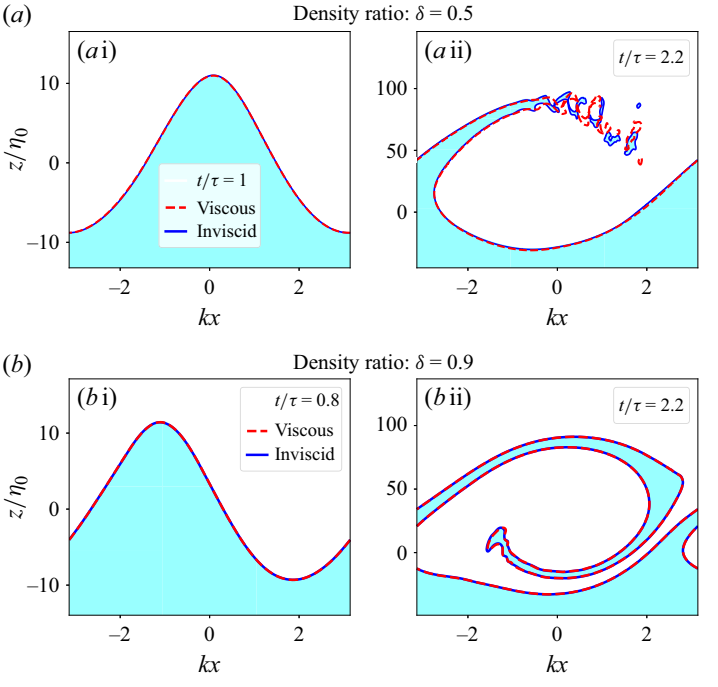


Figure 24. Comparison of inviscid and viscous simulations at the same Bo and Fr. (*a*) Inviscid simulation (as in figure 20) versus a viscous case with perfluorodecalin ($\mu = 5.01$ mPa s, heavier phase) and water ($\mu = 1$ mPa s, lighter phase), with density ratio $\delta = 0.5$. (*b*) Inviscid simulation (as in figure 21) versus a viscous case with brine ($\mu = 1.05$ mPa s, heavier phase) and fresh water ($\mu = 1$ mPa·s, lighter phase), with $\delta = 0.9$. For the viscous results, we solve the incompressible Navier–Stokes equations with kinematic viscosity $\nu > 0$ in both fluids. Viscosity has a relatively minor effect within the time window considered.

that these viscous simulation results are preliminary and are reported for consistency – a careful comparison of the solution to the Rayleigh equation against the numerical solution to the Orr–Sommerfeld equations for the exponential profile is necessary and is currently underway. The viscous simulations have been carried out employing free-slip boundaries, thus ensuring that boundary layers do not develop at the computational boundaries. These simulations are reported in figure 24(*a*,*b*), comparing these against their inviscid counterparts; a good comparison in general is apparent.

5. Effect of change of δ on the background profile: the double exponential profile

So far, we have considered inviscid linear stability of the background shear and density profiles in (2.1), with shear only in the upper fluid. Recall that within the inviscid

https://doi.org/10.1017/jfm.2026.11588 Published online by Cambridge University Press

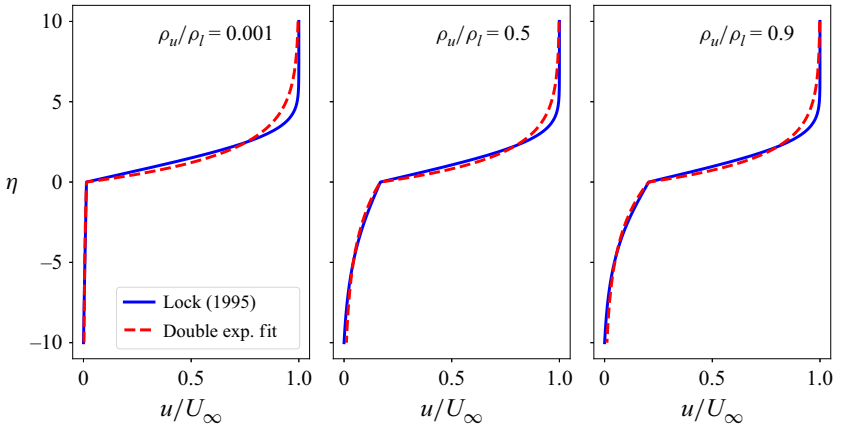


Figure 25. Vertical variation of the horizontal velocity profile with δ, i.e. $u_u/U_\infty = f_1(\eta_1),\ u_l/U_\infty = f_2(\eta_2)$, for fixed viscosity ratio ($\mu^u/\mu^l = 0.02$) corresponding to air–water and $Bo \to \infty$. Note that $\eta = \eta_1$ and η_2 for upper and lower fluids, respectively. The profiles (dashed) are obtained by numerically solving equation (9) (upper layer) and equation (15) (lower layer) in Lock (1951) governing f_1, f_2, subject to boundary conditions provided therein. We choose the far-field velocity in the lower fluid $U_2 = 0$ as $\eta_2 \to -\infty$ (Lock 1951), employing the shooting method. The variable $\eta_1 \equiv y\sqrt{U_\infty/\nu_u x}$ with $\eta_2 = \sqrt{(\nu_u/\nu_l)}\eta_1$. In each case, we fit a double exponential velocity profile of the form provided in expressions (5.1) with the (dimensional) coordinate z in the upper and lower fluids being replaced by (non-dimensional) η_1 and η_2, respectively, and the dimensional variables Δ_u and Δ_l replaced by (non-dimensional) $\mathcal{A}$ and $\mathcal{B}$, respectively. The fitted parameters are (*a*) $U_0 \approx 0.01386$, $\mathcal{A} = 1.1777$, $\mathcal{B} = 5.766$; (*b*) $U_0 \approx 0.1685$, $\mathcal{A} = 1.607$, $\mathcal{B} = 3.659$; (*c*) $U_0 \approx 0.2046$, $\mathcal{A} = 3.408$, $\mathcal{B} = 3.408$. For all three panels and the double exponential profiles in these, $Fr = 4$.

approximation, any shear profile in either fluid (upper or lower) along with a flat density interface ($\eta = 0$) with arbitrary ρ_u, $\rho_l > 0$ and a hydrostatic pressure field is an exact solution to the inviscid momentum and mass equations, as well as the boundary conditions (see § 3 in the supplementary material). In experiments or naturally occurring situations involving viscous, immiscible fluids, one however expects that as the density ratio $\delta \to 1^-$ (such as in this study), the viscous shear stress exerted by the upper fluid on the lower one generates significant momentum transfer to the lower fluid. (We thank an anonymous referee for pointing this out). For the air–water configuration, the importance of viscous shear in either fluids was studied by Valenzuela (1976) in their solution to the Orr–Sommerfeld equation (see their figure 3*b* for the background state). Viscosity, interestingly, can also generate a viscous H instability distinct from the inviscid H instability discussed so far; this was discovered and analysed in Parker *et al.* (2020) for smooth shear and density profiles of the tan hyperbolic form. These results in turn imply that, as $\delta \to 1^-$, for our inviscid linear stability results to be physically relevant and realisable, we need to consider background states with shear in both fluids. This is in contrast to (2.1), which is expected to be an accurate physical representation in the limit of $\delta \to 0$ only.

We demonstrate below that the transition in the nature of instability observed with varying δ for the background state of (2.1) also occurs for profiles with background shear in both fluids. Towards this, we first compute the self-similar velocity profile at the interface of two viscous, immiscible fluids with a flat density interface; this background state seems to have been first reported by Lock (1951). Figure 25 depicts the velocity profile as a function of the similarity coordinate η (see figure caption for a definition) obtained by solving the equations of Lock (1951) (see figure 25 caption for details). Expectedly, as δ is increased (for a fixed viscosity ratio), the background shear in the lower fluid becomes

https://doi.org/10.1017/jfm.2026.11588 Published online by Cambridge University Press

comparable to that in the upper one. In the same figure, for comparison, the 'double exponential' approximation (expression (5.1*a*); Young & Wolfe 2014) to the viscous, self-similar velocity profile of Lock (1951) are also provided. This double exponential profile is given by

$$U(z) = \begin{cases} U_u(z) = U_\infty - (U_\infty - U_0)\exp\left(-\dfrac{z}{\Delta_u}\right), & z > 0, \\ U_l(z) = U_0 \exp\left(\dfrac{z}{\Delta_l}\right), & z < 0, \end{cases} \tag{5.1a}$$

$$\rho(z) = \begin{cases} \rho_u, & z > 0, \\ \rho_l, & z < 0, \end{cases} \tag{5.1b}$$

where U_0 is the background interface velocity at $z = 0$.

Expressions (5.1) generalise the earlier background state of (2.1); setting $U_0 = 0$ in the former recovers the latter. A good qualitative match between the double exponential and the viscous profiles is apparent in figure 25. Note, in particular, that for the air–water density ratio $\delta = 0.001 \ll 1$, the shear in water is negligibly small ($U_0 \approx 0$, leftmost panel of figure 25) and the viscous as well as the double exponential profile are modelled well, by the single exponential profile of (2.1). This is not so at higher $\delta \to 1^-$ (middle and right panels of figure 25) where the background shear in the lower fluid becomes substantial. Our choice of the double exponential profile as an approximation to the self-similar viscous profile (Lock 1951) is partly motivated by the observation that the (inviscid) linear stability problem can also be analytically solved for this profile (Young & Wolfe 2014). This is in contrast to the profile of Lock (1951), for which only numerical solutions to the Rayleigh equation seem feasible. An additional and important advantage is that the change in the sign of $D^2U(z)$ across $z = 0$ for expression (5.1*a*) implies that the KH instability can be expected for this profile in the unstratified limit $\delta = 1$, as a consequence of Rayleigh's inflection point theorem.

Due to the good qualitative match seen between the self-similar, viscous profiles (Lock 1951) and the double exponential profiles in figure 25, we proceed next with the intuitive expectation that linear, inviscid stability results, including transitions in the instability mechanism obtained for the background state (5.1), also apply to the viscous profiles of Lock (1951). We thus examine the inviscid, linear stability of the background state (5.1) as a function of the density ratio δ.

The stability analysis of (5.1) is carried out in an exactly similar manner as § 2 earlier, the only difference being that both fluids now have shear in their background state. The Rayleigh equations in both fluids may be solved for this background state in terms of the Gauss hypergeometric function; we omit details as these can be found in Young & Wolfe (2014). Note that two additional non-dimensional numbers appear for the background state of (5.1*a*), (5.1*b*), *viz.* Δ_l/Δ_u and U_s/U_∞: both these ratios were zero in our analysis so far for the background state of (2.1).

The vertical variation of Reynolds stress and perturbation kinetic energy as a function of δ are depicted in figures 26(*a*) and 26(*b*), respectively. Note that the parameters of the double exponential profile were chosen such that the rippling instability (Young & Wolfe 2014) does not manifest. In figure 26, one notes the same transition in the vertical variation of either metrics as was noted in figure 15 for the single exponential profile. Furthermore, results from nonlinear simulations initialised with eigenfunctions obtained from linear stability analysis of the double exponential profile of (5.1) are shown in figure 27. It thus becomes clear that our earlier results, notably the transition from Miles to the H and eventually to the KH instability, with increasing δ remain applicable also to the

https://doi.org/10.1017/jfm.2026.11588 Published online by Cambridge University Press

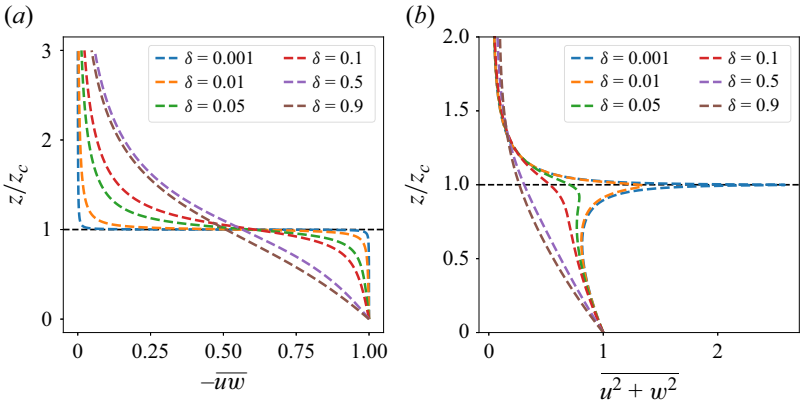


Figure 26. (*a*) Vertical variation of Reynolds stress. (*b*) Perturbation kinetic energy for the double exponential background profile of expressions (5.1). Here $Fr = 4$, $Bo = 87.813$, $\Delta_l/\Delta_u = 0.1$, $U_s/U_\infty = 0.1$.

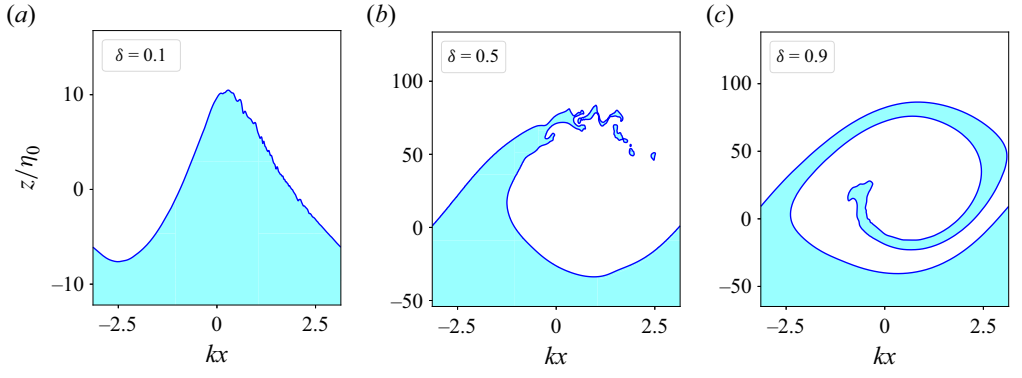


Figure 27. Evolution of the interface initialised with eigenmodes obtained from linear stability analysis of the background state in (5.1). Results are shown for (*a*) $t/\tau = 8.317$, (*b*) $t/\tau = 3.0$ and (*c*) $t/\tau = 2.55$, where τ is the time taken to travel one wavelength. Here $Fr = 4$, $Bo = 87.813$, $\Delta_l/\Delta_u = 0.212$, $U_s/U_\infty = 0.1$.

double exponential background state of (5.1*a*) and (5.1*b*). The applicability of our results, spanning a range of density ratios from very low ($\delta \ll 1$) to close to unity ($\delta \sim O_m(1)$), is thus apparent.

6. Conclusions

In this study we have identified a novel transition in the nature of the fastest growing mode for the exponential profile with a sharp density interface. This transition has been studied at a low Froude number and high Bond number, and is observed with varying density ratio. At $\delta \ll 1$, the fastest growing mode has features typical of the Miles instability (Miles 1957) with a near-discontinuous phase change in the eigenfunction across z_c; the extremely low value of c_i/c_r even for the fastest growing mode in this regime makes it behave nearly like a singular neutral mode (Maslowe & Spiteri 2013), leading to energy extraction only below the critical location and upto the density interface, i.e. a subset of the shear layer. As the density ratio is increased beyond 0.1, the value of c_i/c_r increases proportionally. For a growing mode, while the semi-circle theorem always ensures that $U_u(z_c) = c_r(k)$, the sharp jump in Reynolds stress at z_c gives way

https://doi.org/10.1017/jfm.2026.11588 Published online by Cambridge University Press

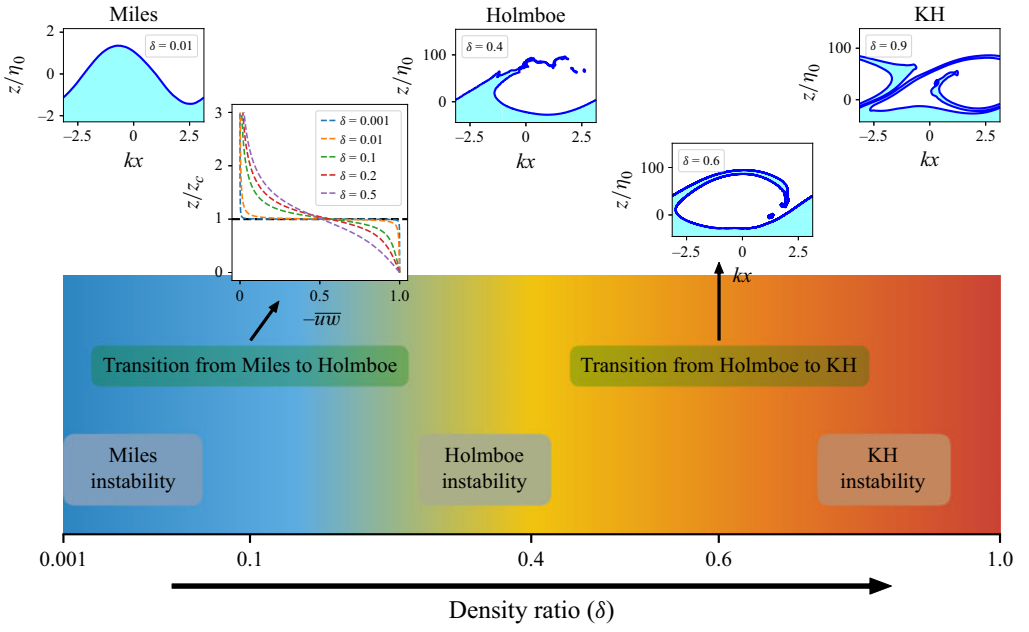


Figure 28. A pictorial summary of key results. The colour contours are informed by results obtained from theory and simulations. These have been generated synthetically, chosen so as to highlight the transition in instability mechanism with increasing δ.

to a smooth variation through z_c, implying energy extraction throughout the shear layer. We rationalise this transition employing an analytical expression for the Reynolds stress, originally due to Lin (1954). The aforementioned smoothing is also shown to occur in the phase of the leading-order term bearing the logarithmic singularity in Tollmien's inviscid, series solutions. At $\delta = 0.5$, we show that the growth rate for the fastest mode compares well against that of the PL profile. This suggests that the transition from the H to KH instability seen in the PL profile with increasing δ can also manifest for the exponential model, albeit modified by the presence of the critical location in the latter. We emphasise that, for the PL profile, due to a lack of profile curvature (except at the corners), the unstable eigenmodes are not singular even though they have a critical layer (see similar observations for stable eigenfunctions in Kadam *et al.* (2023) for the case of a water layer at $\delta = 0$ with a linear shear profile). We have further validated that, for the asymmetric profile under consideration and with increasing δ, the Reynolds stress and perturbation kinetic energy do not bear any signature of a potential transition from the H to KH instability that we anticipate. To establish this, we turn to nonlinear simulations. A pictorial summary of key results is shown in figure 28.

In addition to the excellent validation of linear predictions at least for a few wave periods, our simulations clearly show qualitative differences in the nonlinear regime between $\delta = 0.5$ and $\delta = 0.9$. The former is associated with a finite-amplitude wave with a sheared cusp emitting spume-like droplets from its tip. In marked contrast, at $\delta = 0.9$, nonlinear simulations recover the classic KH spirals. We show that these differences are consistent with the classification scheme proposed in Lawrence *et al.* (1998), distinguishing the H from KH instability for asymmetric profiles.

An important takeaway from our study is the observation that the Miles instability persists for $\delta = 0.01$ (at low Fr and high Bo), i.e. even at ten times the air–water ratio. Given that the growth rate of this instability scales with density ratio, this plausibly makes

https://doi.org/10.1017/jfm.2026.11588 Published online by Cambridge University Press

it easier to experimentally measure growth rates of the Miles instability by exploring fluid combinations other than air–water. Our study also reports several comparisons against the PL profile in high- and low-*Fr* regimes, establishing the qualitative role of background profile curvature. The role of viscosity requires careful analysis involving the Orr–Sommerfeld equation. This is underway and will be reported subsequently.

Supplementary material. Supplementary material is available at https://doi.org/10.1017/jfm.2026.11588.

Acknowledgements. R.D. acknowledges Professor Anubhab Roy for suggesting the Holmboe instability at the early stage of this study. Figure 19(*c*) was generated by Nikhil Yewale and is acknowledged. We thank the organisation of the International Research Network (IRN) under the auspice of CNRS for the workshop held at Univ. Paris, Saclay, France in June 2025 where this work was presented. We thank Professor Herbert E. Huppert for helpful comments. We thank the anonymous referees for several helpful remarks concerning interpretations in terms of wave interactions.

Funding. We gratefully acknowledge financial support from DST-SERB (Govt. of India) grants MTR/2019/001240, CRG/2020/003707, SPR/2021/000536, MoE-STARS/STARS-2/2023-0595 on various problems concerning nonlinear ocean waves, wave breaking and spray formation. S.R. is supported through IIT Bombay Seed Grant RD/0522-IRCCSH0-020. The Ph.D. tenure of A.K. is supported by the SERB grant (CRG/2020/003707) and is gratefully acknowledged. Computational time on the IIT Bombay High Performance Computing (HPC) facility is gratefully acknowledged.

Declaration of interests. The authors report no conflict of interest.

References

Alexakis, A., Calder, A.C., Dursi, L.J., Rosner, R., Truran, J.W., Fryxell, B., Zingale, M., Timmes, F.X., Olson, K. & Ricker, P. 2004*a* On the nonlinear evolution of wind-driven gravity waves. *Phys. Fluids* **16** (9), 3256–3268.

Alexakis, A., Young, Y. & Rosner, R. 2002 Shear instability of fluid interfaces: stability analysis. *Phys. Rev. E* **65** (2), 026313.

Alexakis, A., Young, Y.-N. & Rosner, R. 2004*b* Weakly nonlinear analysis of wind-driven gravity waves. *J. Fluid Mech.* **503**, 171–200.

Andrews, G.E., Askey, R. & Roy, R. 1999 *Special Functions*. Cambridge University Press.

Baines, P.G. & Mitsudera, H. 1994 On the mechanism of shear flow instabilities. *J. Fluid Mech.* **276**, 327–342.

Barros, R. & Choi, W. 2011 Holmboe instability in non-Boussinesq fluids. *Phys. Fluids* **23** (12), 124103.

Benjamin, T.B. 1960 Effects of a flexible boundary on hydrodynamic stability. *J. Fluid Mech.* **9** (4), 513–532.

Benjamin, T.B. 1963 The threefold classification of unstable disturbances in flexible surfaces bounding inviscid flows. *J. Fluid Mech.* **16** (3), 436–450.

Bonfils, A.F., Mitra, D., Moon, W. & Wettlaufer, J.S. 2022 Asymptotic interpretation of the Miles mechanism of wind-wave instability. *J. Fluid Mech.* **944**, A8.

Boomkamp, P.A.M. & Miesen, R.H.M. 1996 Classification of instabilities in parallel two-phase flow. *Intl J. Multiphase Flow* **22**, 67–88.

Carpenter, J.R., Balmforth, N.J. & Lawrence, G.A. 2010 Identifying unstable modes in stratified shear layers. *Phys. Fluids* **22** (5), 054104.

Carpenter, J.R., Guha, A. & Heifetz, E. 2017 A physical interpretation of the wind-wave instability as interacting waves. *J. Phys. Oceanogr.* **47** (6), 1441–1455.

Carpenter, J.R., Tedford, E.W., Heifetz, E. & Lawrence, G.A. 2011 Instability in stratified shear flow: review of a physical interpretation based on interacting waves. *Appl. Mech. Rev.* **64** (6), 060801.

Cavaleri, L., *et al.* 2007 Wave modelling – The state of the art. *Prog. Oceanogr.* **75** (4), 603–674.

Cohen, L.S. & Hanratty, T.J. 1965 Generation of waves in the concurrent flow of air and a liquid. *AIChE J.* **11** (1), 138–144.

Cushman-Roisin, B. & Beckers, J.-M. 2011 *Introduction to Geophysical Fluid Dynamics: Physical and Numerical Aspects*. International Geophysics, vol. 101, 2nd edn. Academic Press.

Deike, L. 2022 Mass transfer at the ocean–atmosphere interface: the role of wave breaking, droplets, and bubbles. *Annu. Rev. Fluid Mech.* **54** (1), 191–224.

Drazin, P.G. & Reid, W.H. 2004 *Hydrodynamic Stability*. Cambridge University Press,

Eaves, T.S. & Balmforth, N.J. 2019 Instability of sheared density interfaces. *J. Fluid Mech.* **860**, 145–171.

https://doi.org/10.1017/jfm.2026.11588 Published online by Cambridge University Press

FRITTS, D.C. & ALEXANDER, M.J. 2003 Gravity wave dynamics and effects in the middle atmosphere. *Rev. Geophys.* **41** (1), 1003.
GARRETT, C. & MUNK, W. 1979 Internal waves in the ocean. *Annu. Rev. Fluid Mech.* **11** (1), 339–369.
GOLDSTEIN, S. 1931 On the stability of superposed streams of fluids of different densities. *Proc. R. Soc. Lond. Ser. A, Contain. Pap. Math. Phys. Charact.* **132** (820), 524–548.
HABERMAN, R. 1972 Critical layers m parallel flows. *Stud. Appl. Math.* **51** (2), 139–161.
Helmholtz 1868 XLIII. On discontinuous movements of fluids. *Lond. Edinb. Dublin Phil. Mag. J. Sci.* **36** (244), 337–346.
HOLMBOE, J. 1962 On the behavior of symmetric waves in stratified shear layers. *Geofysiske Publikasjoner* **24**, 67–113.
HUNG, L.-P. & TSAI, W.-T. 2009 The formation of parasitic capillary ripples on gravity–capillary waves and the underlying vortical structures. *J. Phys. Oceanogr.* **39** (2), 263–289.
JANSSEN, P.A.E.M. 2008 Progress in ocean wave forecasting. *J. Comput. Phys.* **227** (7), 3572–3594.
JEFFREYS, H. 1925 On the formation of water waves by wind. *Proc. R. Soc. Lond. Ser. A Contain. Pap. Math. Phys. Charact.* **107** (742), 189–206.
JOHANSSON, F. 2024 mpmath: a python library for arbitrary-precision floating-point arithmetic. Available at: http://mpmath.org/. version 1.3.0, using findroot with Müller's method,
KADAM, Y., PATIBANDLA, R. & ROY, A. 2023 Wind-generated waves on a water layer of finite depth. *J. Fluid Mech.* **967**, A12.
KAYAL, L., SANJAY, V., YEWALE, N., KUMAR, A. & DASGUPTA, R. 2025 Focussing of concentric free-surface waves. *J. Fluid Mech.* **1003**, A14.
KUMAR, A. 2025 Basilisk c simulation: two-phase shear flow. Available at: https://github.com/a-k-sangwan/Basilisk-Codes/tree/main/Shear-flow.
LAWRENCE, G.A., BROWAND, F.K. & REDEKOPP, L.G. 1991 The stability of a sheared density interface. *Phys. Fluids A: Fluid Dyn.* **3** (10), 2360–2370.
LAWRENCE, G.A., HAIGH, S.P. & ZHU, Z. 1998 In search of Holmboe's instability. *Phys. Process. Lakes Oceans* **54**, 295–304.
LEBLANC, S. 2007 Amplification of nonlinear surface waves by wind. *Phys. Fluids* **19** (10), 101705.
LIGHTHILL, M.J. & ROSENHEAD, L. 1963 *Laminar Boundary Layers*, pp. 5–88. Oxford University Press.
LIN, C.C. 1954 Some physical aspects of the stability of parallel flows. *Proc. Natl Acad. Sci.* **40** (8), 741–747.
LOCK, R.C. 1951 The velocity distribution in the laminar boundary layer between parallel streams. *Q. J. Mech. Appl. Math.* **4** (1), 42–63.
MASLOWE, S.A. & SPITERI, R.J. 2013 A study of singular modes associated with over-reflection and related phenomena. *J. Fluid Mech.* **728**, 120–145.
MATAS, J.-P., MARTY, S. & CARTELLIER, A. 2011 Experimental and analytical study of the shear instability of a gas–liquid mixing layer. *Phys. Fluids* **23** (9), 094112.
MERCIER, M.J., VASSEUR, R. & DAUXOIS, T. 2011 Resurrecting dead-water phenomenon. *Nonlinear Proc. Geophys.* **18** (2), 193–208.
MICHALKE, A. 1964 On the inviscid instability of the hyperbolictangent velocity profile. *J. Fluid Mech.* **19** (4), 543–556.
MILES, J.W. 1957 On the generation of surface waves by shear flows. *J. Fluid Mech.* **3** (2), 185–204.
MILES, J.W. 1959 On the generation of surface waves by shear flows Part 3. Kelvin–Helmholtz instability. *J. Fluid Mech.* **6** (4), 583–598.
MILES, J.W. 1962 On the generation of surface waves by shear flows. Part 4. *J. Fluid Mech.* **13** (3), 433–448.
MITSUYASU, H. 2002 A historical note on the study of ocean surface waves. *J. Oceanogr.* **58**, 109–120.
MORLAND, L.C. & SAFFMAN, P.G. 1993 Effect of wind profile on the instability of wind blowing over water. *J. Fluid Mech.* **252**, 383–398.
MÜLLER, D.E. 1956 A method for solving algebraic equations using an automatic computer. *Math. Tables Other Aids Comput.* **10** (56), 208–215.
MORLAND, L.C., SAFFMAN, P.G. & YUEN, H.C. 1991 Waves generated by shear layer instabilities. *Proc. R. Soc. Lond. Ser. A: Math. Phys. Sci.* **433** (1888), 441–450.
PARKER, J.P., CAULFIELD, C.-C.P. & KERSWELL, R.R. 2020 The viscous Holmboe instability for smooth shear and density profiles. *J. Fluid Mech.* **896**, A14.
PELTIER, W.R. & CAULFIELD, C.P. 2003 Mixing efficiency in stratified shear flows. *Annu. Rev. Fluid Mech.* **35** (1), 135–167.
PERLIN, M., CHOI, W. & TIAN, Z. 2013 Breaking waves in deep and intermediate waters. *Annu. Rev. Fluid Mech.* **45** (1), 115–145.
PIZZO, N., DEIKE, L. & AYET, A. 2021 How does the wind generate waves? *Phys. Today* **74** (11), 38–43.

https://doi.org/10.1017/jfm.2026.11588 Published online by Cambridge University Press

POPINET, S. 2003 Gerris: a tree-based adaptive solver for the incompressible Euler equations in complex geometries. *J. Comput. Phys.* **190** (2), 572–600.
POPINET, S. & Collaborators 2013–2025 An adaptive mesh refinement algorithm for the incompressible Navier–Stokes equations using vof method. Available at: http://basilisk.fr.
POULIQUEN, O., CHOMAZ, J.M. & HUERRE, P. 1994 Propagating Holmboe waves at the interface between two immiscible fluids. *J. Fluid Mech.* **266**, 277–302.
Rayleigh 1895 On the stability or instability of certain fluid motions (III.). *Proc. Lond. Math. Soc.* **1** (1), 5–12.
RUBAN, A., GAJJAR, J. & WALTON, A. 2023 *Fluid Dynamics: Part 4: Hydrodynamic Stability Theory*. Oxford University Press.
RUSSELL, J.M. 1994 A survey of exact solutions of inviscid field equations in the theory of shear flow instability. *Appl. Sci. Res.* **53**, 163–186.
SHELTON, J., MILEWSKI, P. & TRINH, P.H. 2025 Time-dependent nonlinear gravity–capillary surface waves with viscous dissipation and wind forcing. *J. Fluid Mech.* **1003**, A13.
SHRIRA, V.I. 1993 Surface waves on shear currents: solution of the boundary-value problem. *J. Fluid Mech.* **252**, 565–584.
SMYTH, W.D. & PELTIER, W.R. 1989 The transition between Kelvin–Helmholtz and Holmboe instability: an investigation of the overreflection hypothesis. *J. Atmos. Sci.* **46** (24), 3698–3720.
SMYTH, W.D. & WINTERS, K.B. 2003 Turbulence and mixing in Holmboe waves. *J. Phys. Oceanogr.* **33** (4), 694–711.
STAQUET, C. & SOMMERIA, J. 2002 Internal gravity waves: from instabilities to turbulence. *Annu. Rev. Fluid Mech.* **34** (1), 559–593.
STERN, M.E. 1973 Capillary waves generated by a shear current in water. *Mem. Soc. R. Sci. Liege* **6** (6), 179.
STEWARTSON, K. 1981 Marginally stable inviscid flows with critical layers. *IMA J. Appl. Math.* **27** (2), 133–176.
TAYLOR, G.I. 1931 Effect of variation in density on the stability of superposed streams of fluid. *Proc. R. Soc. Lond. Ser. A Contain. Pap. Math. Phys. Charact.* **132** (820), 499–523.
THOMSON, W. 1871 Xlvi. Hydrokinetic solutions and observations. *Lond. Edinb. Dublin Phil. Mag. J. Sci.* **42** (281), 362–377.
THORPE, S.A. 1975 The excitation, dissipation, and interaction of internal waves in the deep ocean. *J. Geophys. Res.* **80** (3), 328–338.
TOLLMIEN, W. 1935 Ein allgemeines kriterium der instabilitat laminarer gescgwindigkeits-verteilungen. *Nachr. Wiss Fachgruppe, Göttingen, Math. Phys.* **1**, 79.
TRYGGVASON, G.ÉTAR, SCARDOVELLI, R. & ZALESKI, S.ÉPHANE 2011 *Direct Numerical Simulations of Gas–Liquid Multiphase Flows*. Cambridge University Press.
VALENZUELA, G.R. 1976 The growth of gravity-capillary waves in a coupled shear flow. *J. Fluid Mech.* **76** (2), 229–250.
YIH, C.-S. 1960 Gravity waves in a stratified fluid. *J. Fluid Mech.* **8** (4), 481–508.
YIH, C.-S. 1972 Surface waves in flowing water. *J. Fluid Mech.* **51** (2), 209–220.
YOUNG, W.R. & WOLFE, C.L. 2014 Generation of surface waves by shear-flow instability. *J. Fluid Mech.* **739**, 276–307.

https://doi.org/10.1017/jfm.2026.11588 Published online by Cambridge University Press